

**Fluid Structure Interaction Analysis of a Wind Turbine Blade with Bend-Twist Coupling for
Performance Enhancement**

by © Mehdi Masoudi

A Thesis submitted to the School of Graduate Studies
in partial fulfillment of the requirements for the degree of

Master of Engineering

Memorial University of Newfoundland

September, 2018

St. John's Newfoundland and Labrador

Abstract

This research aims to investigate the aeroelastic capacities of a blade through geometry based bend twist coupling (BTC). Power optimization is performed based on Blade Element Momentum Theory (BEMT) on NREL phase VI rotor and optimized power and elastic twist curves are presented. Elastic twist of the blade can be tailored to improve blade performance. BTC is implemented through the blade spar and blade planform. An L beam is incorporated in the blade as spar and fluid-structure interaction analysis is conducted. 1-way and 2-way fluid-structure interaction analysis are performed and compared. CFD results are verified with experimental data. Induced elastic twist is presented for different spar thicknesses and spar locations over a range of wind speeds. The results show improved elastic twist with a thicker spar placed closer to the tip of the blade. Modified blade designs with different curved planform are analyzed and the results are presented in this thesis. The curved blade is modeled and analyzed with L spar and box spar to compare the effects of spar type on elastic twist. More elastic twist is predicted in the blade with L spar compared to the blade with box spar. Elastic twist of up to 0.7° is yielded from the curved blades with L spar with bend depth of 1.5 m. A power increase of 1.89% for the wind turbine due to the induced elastic twist is predicted.

Acknowledgement

I would like to greatly appreciate Dr. Kevin Pope's supervision and financial support during my studies as a master student at Memorial University. I would also like to greatly appreciate Dr. Sam Nakhla's advice in this research.

Table of Contents

Abstract.....	ii
Acknowledgement.....	iii
List of Tables.....	vi
List of Figures.....	vii
Abbreviations and symbols.....	x
1 Background.....	1
1.1 Introduction.....	1
1.2 Power control in wind turbines.....	2
1.3 Power control methods.....	3
1.4 Aeroelastic tailoring.....	9
1.5 Objectives and Overview of Thesis.....	12
2 Formulation of bend-twist coupling.....	14
2.1 Blade Element Momentum Theory and Optimization.....	14
2.2 Spar Selection.....	27
2.3 Fluid Structure Interaction.....	34
2.4 Measuring elastic twist.....	36
3 Results and Discussion.....	38
3.1 Angle beam bend twist coupling potential.....	38
3.2 Orientation of spar.....	40
3.3 Locating NREL S809 airfoil center of pressure.....	40

3.4 2D CFD verification.....	41
3.5 FSI model.....	44
3.5.1 CFD model.....	44
3.5.2 FE Model	49
3.6 Two-way Vs. one-way FSI.....	50
3.7 Elastic twist	51
3.8 Swept blade	54
3.8.1 Curved planform	54
3.8.2 Elastic twist	56
3.8.3 Comparison of predicted elastic twist with optimal twist angle	60
3.8.4 Power increase.....	61
4 Conclusions and recommendations.....	63
4.1 Conclusions	63
4.2 Recommendations for future studies	64
References	65

List of Tables

Table 1. Blade chord and twist distribution [47]	22
Table 2. Finite element mesh independence study for angle beam	39
Table 3. Twist of the beam at the tip.....	40
Table 4. Elastic static structural response of angle beams.....	40
Table 5. Location of center of pressure	41
Table 6. Mesh independence study for 2D C-grid	41
Table 7. Mesh independence study for the 3D rectangular domain.....	47
Table 8. Power change.....	62

List of Figures

Figure 1. Typical wind turbine power curve	3
Figure 2. Turbine control techniques.....	4
Figure 3. Power output of a stall controlled wind turbine [5]	5
Figure 4. Effect of blade pitch angle on power output in a constant speed rotor [5].....	7
Figure 5. Extendible blade [6]	7
Figure 6. Streamlines around a microtab mounted on suction side of S809 airfoil [6]	8
Figure 7. Variations of Bend Twist Coupling.....	11
Figure 8. Biased fibers.....	11
Figure 9. Swept blade planform [45]	11
Figure 10. Streamlines passing through a wind turbine [5].....	14
Figure 11. The trajectory of an air particle passing through the rotor disc [5]	15
Figure 12. Wind turbine and blade section	15
Figure 13. Aerodynamics of a typical wind turbine for (a) blade section velocities (b) and forces (modified from [5])	16
Figure 14. Induction factors at wind speed $U_{\infty} = 8 \text{ m/s}$	19
Figure 15. Rotor power versus wind speed	19
Figure 16. Optimized power	21
Figure 17. Chord distribution [47]	22
Figure 18. Twist angle distribution [47]	23
Figure 19. Optimal pitch angles for maximum power output at various wind speeds	23
Figure 20. Optimal pitch angle for maximum power output at $U_{\infty} = 8 \text{ m/s}$ and $U_{\infty} = 5 \text{ m/s}$	24

Figure 21. Blade section forces and angles.....	25
Figure 22. Desired elastic twist for $U_\infty = 8 \text{ m/s}$	26
Figure 23. Optimal angle of attack at $U_\infty = 8 \text{ m/s}$	27
Figure 24. Finding optimized angle of attack.....	27
Figure 25. Wind turbine blade components.....	28
Figure 26. Different Spar designs.....	28
Figure 27. Shear flow in a box section	29
Figure 28. Closed and open rectangular sections.....	30
Figure 29. Channel section.....	30
Figure 30. Schematic of spar section	31
Figure 31. Lift and drag forces at the center of pressure	32
Figure 32. Blade cross section free body diagram.....	33
Figure 33. Spar orientations with the cap facing (a) right and (b) left.....	33
Figure 34. Numerical solution methods for Fluid Solid Interaction problems	34
Figure 35. One way and two way FSI	35
Figure 36. schematic of the blade section after and before deformation	37
Figure 37. Angle beam	38
Figure 38. Angle section beam flapwise deformation.....	39
Figure 39. Grid around the airfoil	43
Figure 40. Coefficient of pressure for $\alpha = 9^\circ$ at $Re=1 \text{ million}$	44
Figure 41. Wind velocity vectors on the blade	45
Figure 42. C-domain and boundary conditions	46

Figure 43. Rectangular domain mesh	47
Figure 44. Coefficient of pressure for $\alpha = 15^\circ$ at $Re=1$ million	48
Figure 45. Blade mesh.....	49
Figure 46. Blade deformation.	51
Figure 47. Induced elastic twist for different wind speeds for spar located at $x = 0.2c$	52
Figure 48. Elastic twist for different spar locations at $U_\infty = 20$ m/s.....	53
Figure 49. Effect of thickness on elastic twist. $x = 0.1c$, $U_\infty = 20$ m/s	54
Figure 50. Modified curved blade planform	55
Figure 51. Swept blade with box spar.....	55
Figure 52. Cross section of the blade with (a) L spar and (b) Box spar.....	55
Figure 53. Flapwise bending	56
Figure 54. Elastic twist for swept blades	57
Figure 55. Induced twist of blade with L spar and bend depth of 1 m.....	58
Figure 56. Induced twist of blade with L spar at $U_\infty = 10$ m/s	58
Figure 57. Induced twist of blade with L spar at $U_\infty = 15$ m/s	59
Figure 58. Induced twist for bend depth = 1 m at $U_\infty = 10$ m/s.....	60
Figure 59. Induced twist for bend depth = 1 m at $U_\infty = 15$ m/s.....	60
Figure 60. Elastic twist for blade with bend depth of 1.5 m and L spar at $U_\infty = 10$ m/s.....	61

Abbreviations and symbols

r	Blade section Radial distance from the hub [m]
Ω	Turbine rotational velocity [rpm]
U_∞	Wind velocity [m/s]
a	axial flow induction factor [-]
a'	tangential flow induction factor [-]
α	Angle of attack ($^\circ$)
w	Relative wind velocity [m/s]
φ	Angle between relative wind velocity and the plane of blade rotation ($^\circ$)
L	Lift force [N]
D	Drag force [N]
F	Force [N]
C_l	Lift coefficient [-]
C_d	Drag coefficient [-]
ρ	Air density [kg/m ³]
A	Blade section area [m ²]
c	Chord length [m]
λ_r	Section tip speed ratio [-]
P	Power [kW]
B	Number of blades [-]
R	Blade radius [m]
σ'	Chord solidity [-]
δ_T	Section torque [N.m]

δ_P	Section power [kW]
$\theta_{P,0}$	Blade pitch angle (°)
θ_P	Section pitch angle (°)
θ_T	Blade twist angle (°)
θ_e	Elastic twist angle (°)
q	Shear flow [N/m]
d	Lever arm (perpendicular distance) from shear center to load on the spar section [m]
F	Force [N]
s	Perpendicular distance between airfoil center of pressure and spar shear center [m]
ω	Distributed load [N/m]
E	Modulus of elasticity [pa]
ν	Poisson's ratio [-]
γ	Diffusion coefficient [-]
x	Mesh node coordinate [m]
\vec{u}	Mesh displacement velocity vector [m/s]
Δt	Time increment [s]
θ_p'	Section pitch angle after deformation (°)
y	Displacement in y direction [m]
TSR	Tip speed ratio [-]
BTC	Bend twist coupling
COE	Cost of energy
STAR	Sweep-twist adaptive rotor

BET	Blade element theory
HAWT	Horizontal axis wind turbine
BEM	Blade element momentum theory
CFD	Computational fluid dynamics
FEA	Finite element analysis
FBD	Free body diagram
FE	Finite element
C.P.	Center of pressure
Re	Reynolds number [-]
FSI	Fluid structure interaction

1 Background

1.1 Introduction

Renewable energy has gained attention during the past few decades due to increased world energy demand and climate change mitigation strategies. World population is growing by 1.1% per year (2017) [1] and the total energy consumption has increased by 11.3% from 2008-2015 [2, 3]. The greenhouse effect from burning fossil fuels such as oil, gas and coal as main sources of energy have resulted in 0.9 °C [4] temperature rise since 1880. A clean renewable alternative energy source that can address these concerns is wind power. Wind that is driven by uneven solar heating of the earth, is renewable and well distributed around the globe, making it a promising clean energy source.

Wind power technology has developed over the past century and is considered a mature technology. However, there is always a tendency for larger turbines because bigger machines harness more power with lower cost of energy (COE). There are design and manufacturing challenges associated with longer blades. Greater aerodynamic and inertial loads are applied on larger blades, thus stronger structures are needed to withstand the loads. As wind turbines are rotating machines, they experience complex loading which can result in fatigue failures. Reducing load while expanding in size is a major challenge in wind turbines. Power control techniques have been developed over the past years to partly address these issues while there could still be more improvement.

Most current wind turbines use active power control systems, which have expensive elements such as sensors, processors and actuators. These systems suffer from long response time as the blades are very massive and have high inertia. Passive adaptive blades can be used

along with active controls to improve turbine performance. In this thesis, aeroelastic tailoring of a wind turbine blade is studied and the resulted power improvements are reported.

1.2 Power control in wind turbines

Power in wind is proportional to wind velocity to power 3. However, not all of that power can be extracted. Betz's law explains that to capture wind power, there must still be some energy left after it passes through any sort of actuator disk. Based on continuity and conservation of momentum, Betz derived a theoretical maximum for how much power we can extract from wind. According to Betz's law, it is impossible to extract more than $16/27$ (59.3%) of wind power regardless of the type of machine used [5]. Modern wind turbines benefiting from sophisticated power control methods can capture up to 80% of the Betz limit.

Wind speed constantly changes which affects the power coefficient of a turbine. Also, working in excessively high wind conditions can not only damage the turbine, it is not economical as it increases maintenance costs. As there are no controls over incoming wind speeds, some sort of power control method is needed for any type of wind turbine. Simpler control methods such as stall control are used in smaller wind turbines while multiple sophisticated methods are employed in larger rotors (where it is economical) [6]. The goal of wind turbine control is to 1) limit torque and power in excessive wind speeds 2) reduce fatigue, and 3) maximize power production [7].

As illustrated in Figure 1, there is no power production in Region 1 as low wind velocity does not produce enough power to overcome internal losses and friction. In Region 2, the turbine starts producing power as there is more power in the wind. At speeds above rated, in Region 3, the turbine produces rated power which must be maintained as wind speed increases

(until cut-out). Depending on the operating region of the turbine, there are different control objectives and strategies. In Region 2, while the turbine is still operating below its rated power, the control objective is to maximize power output, however, upon reaching its rated power in Region 3, the objective is to limit power output to its rated value and reduce mechanical loads. A turbine should not be working to produce more power than its rated power as this increases cost of energy and puts too much load on the gearbox and generator. When wind reaches over the cut-out speed, the objective is to minimize the aerodynamic load applied on the turbine structure while the rotor is not rotating and brakes are active.

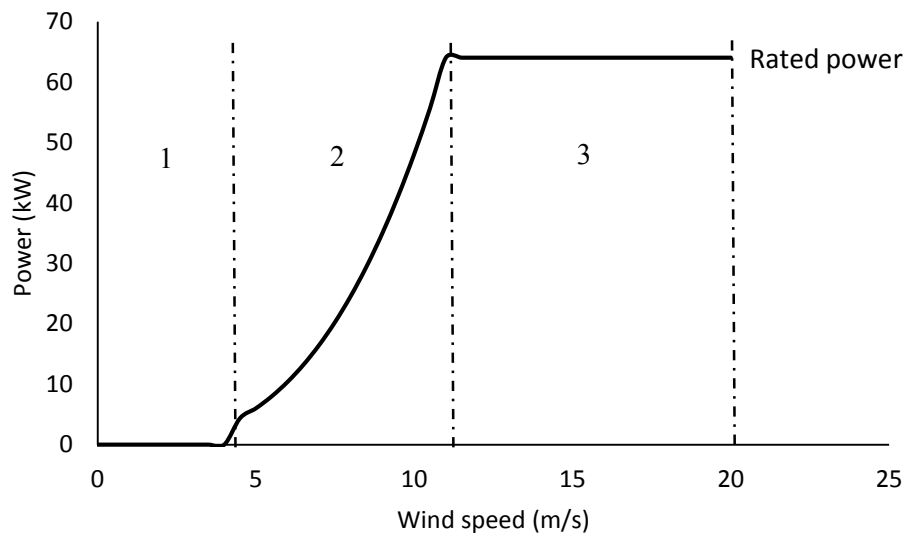


Figure 1. Typical wind turbine power curve

1.3 Power control methods

Turbine control can be divided into active and passive categories. Active methods use sensors and actuators and need external energy. Examples of active controls are the variable speed rotor and blade pitch control. In passive methods, however, there is no need for any

energy expenditure [6]. An example of passive control is stall control. A list of active and passive control methods is shown in Figure 2.

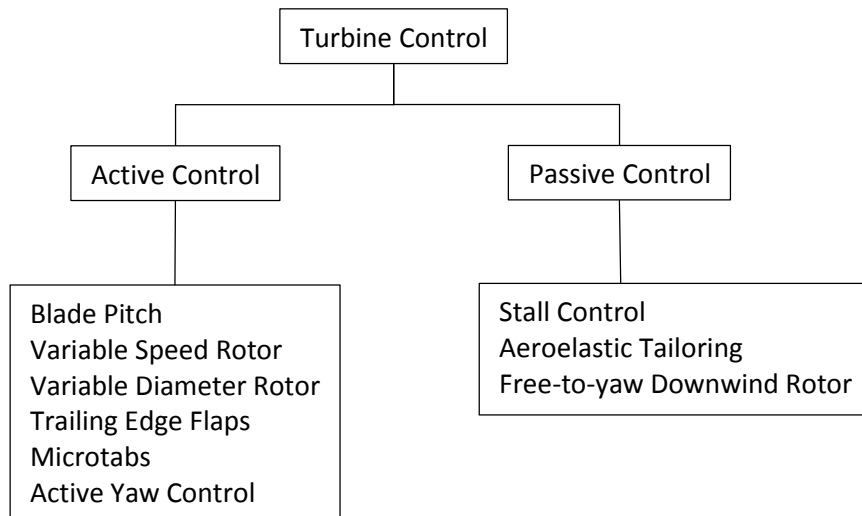


Figure 2. Turbine control techniques

Passive stall control is used in older turbines and modern smaller turbines with constant rotor speeds. This method only depends on the blade aerodynamic characteristics. Stall occurs when the angle of attack exceeds a critical value resulting in a reduction in lift. The airfoils are designed to stall in high winds to reduce aerodynamic loads and torque on the rotor. Different sections of the blade stall at different wind speeds depending on their section pitch angle providing a smooth reduction in torque. Pitch angle is the angle between chord line of the blade section (airfoil) and the plane of the blade rotation. Pitch angle is illustrated graphically in section 2.1. This parameter (section pitch angle) is optimized for each section based on the rotor rated speed and the wind speed history of the located site and is built in the blade. This provides passive control over power production and reduces aerodynamic loads at high winds. Passive stall control is cheaper and simpler, however, the controllability is limited and power

fluctuations and torque spikes are more frequent. Passive stall control is not economical in larger wind turbines [6].

A typical power curve for a stall controlled turbine is shown in Figure 3. As can be seen, once wind speed exceeds the rated 10 m/s, the power drops because the blade starts to stall. Stall starts from the root and as wind speed increases, further sections of the blade also stall, resulting in a smooth reduction in torque and power. In a constant speed rotor, the angle of attack of each blade section is only a function of wind speed.

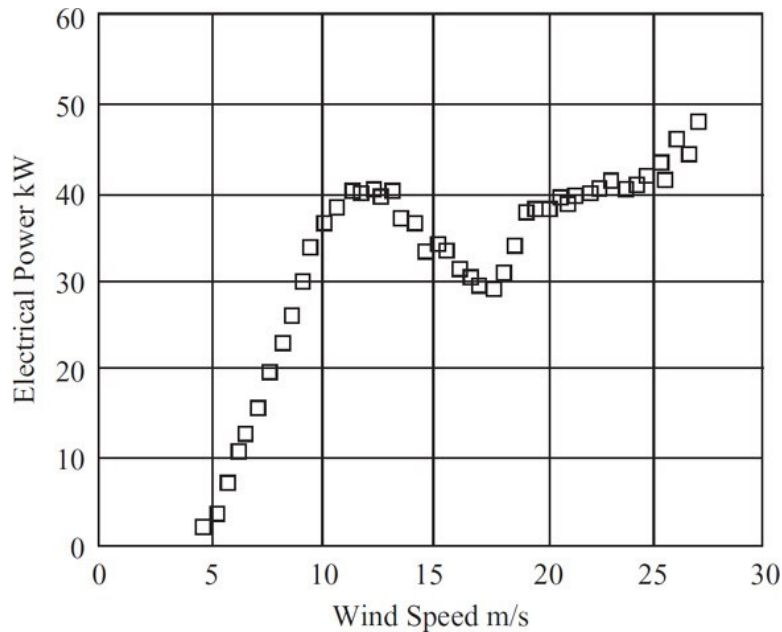


Figure 3. Power output of a stall controlled wind turbine [5]

Modern larger wind turbines use two active control methods: variable speed rotor and blade pitch control. Variable speed technology works by changing generator torque which can slow down or speed up the rotor. In pitch control, the blade can actively rotate around its axis to adjust its pitch angle at different wind speeds. Pitching the blade changes the angle of attack for each section of the blade and results in reduced or increased lift and drag which changes

the load and torque on the blade. Depending on the region and the objective, either blade pitch or rotor speed are the active control regime. In Region 2, where maximizing the power is the objective, rotor speed is active and maintains the optimum tip speed ratio (TSR), which by definition is the speed of blade tip divided by wind speed ($TSR = \frac{r\Omega}{U_\infty}$) [8]. In Region 3, where limiting power to reduce mechanical loads is the objective, the pitch control is active while rotor speed is kept constant [8]. Changing the pitch angle controls the input torque from wind and regulates the power output and mechanical loads. Pitch angle control works by keeping the rotor speed constant thereby power output stays at its rated power.

To further illustrate the effects of pitch angle on power output, a plot of power curves for different pitch angles in a constant rotor speed turbine is shown in Figure 4. For speeds below rated, optimum pitch angle does not change with increasing wind. This is why only variable speed rotor is used for power optimization in this region. In speeds higher than rated, however, constant power output can be achieved by increasing pitch angle as wind speed rises. As can be seen, high pitch angles are needed for power regulation at high wind speeds. This is a disadvantage of the pitch control method.

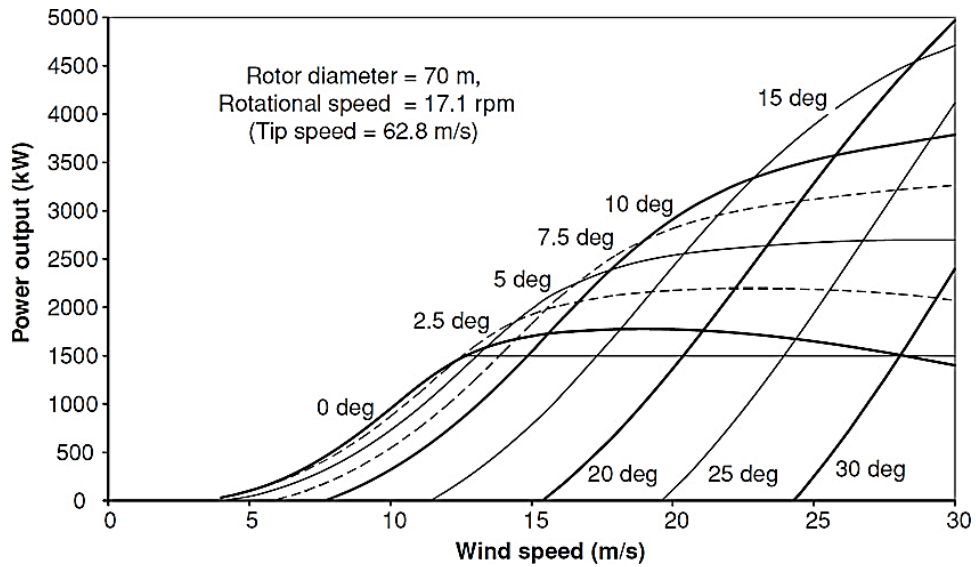


Figure 4. Effect of blade pitch angle on power output in a constant speed rotor [5]

Variable diameter rotor is another concept in active load control which works by changing the blade sweep area [9-13]. Designing a narrow *tip* blade that can be extended and retracted from the inside of a *root* blade makes it possible to create variable length blades (Figure 5) [6]. The tip blade can be extended in low winds to increase the sweep area which increases the power output. In high winds, the tip blade retracts and sheds excessive loads. Power regulation is achieved with pitch control. Prototypes of variable diameter rotors have been built and tested. Tests show a 12.9% increase in power production and a 33% reduction in peak loads compared to standard blades of the same size [9].

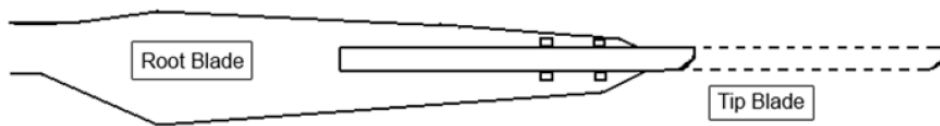


Figure 5. Extendible blade [6]

The concept of using microtabs as a means of load control in wind turbines was first developed by Yen et al [14-16]. Microtabs can be utilized on both sides of the blade with contrary effects. Implementing a tab on the suction side of an airfoil mounted perpendicular to the surface increases the lift coefficient. However, a tab on the pressure side decreases the lift coefficient. By designing tabs of variable heights with translational movement a method of flow control and consequently load control will be achieved. Experimental and numerical studies on GU25-5(11)8 airfoil show an increase of 30-50% in lift with tabs mounted on the suction side [14]. The same study and another similar study on NREL S809 airfoil find that a tab of 1% chord in height located at $x/c = 95$ provides optimum performance [14, 17, 18]. Microtabs work by shifting the point of separation and effectively changing the blade camber. Microtabs are also presented and studied as a passive load control technique [19]. Figure 6 shows the streamline around an airfoil with Microtabs.

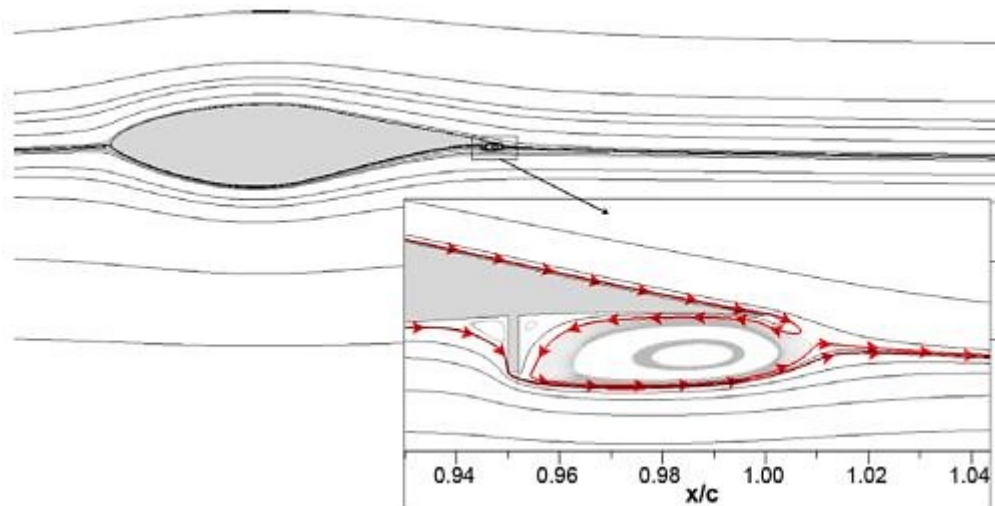


Figure 6. Streamlines around a microtab mounted on suction side of S809 airfoil [6]

1.4 Aeroelastic tailoring

Aeroelastic tailoring is the employment of directional stiffness in aerodynamic structures to control aeroelastic deformations such that the structural response improves the aerodynamic and structural performance [20]. This concept has been used in helicopter and wind turbine industries [21]. Aeroelastic tailoring that is also defined as passive aeroelastic control [22], can be achieved through bend twist coupling (BTC). Bend-induced twist changes the angle of attack for each blade section and the applied torque. The bend-induced elastic twist can be utilized to 1) control load / power and 2) optimize power production. An elastic twist toward stall will alleviate gust loads while twist toward feather can increase power output in low wind speeds. Previous work has shown the potential for modifying blade designs to incorporate bend-twist coupling [23-32].

Stoddard [33] measured a 2.5° elastic twist in wind blades. He suggested that this elastic twist can be employed to our benefit when designing blades. Calculations by Malcolm [34], Lobitz [35] and Verelst [36] indicate fatigue load reduction by employing BTC. Berry [37] reports 2.4-8.6% reduction in the bending load with a 4° elastic twist. Malcolm [34] reports 2% reduction in the Cost of Energy (COE) due to twist coupling. Karaolis [38, 39] first introduced the use of biased fibers in the blade skin to create BTC. Koojiman [40] finds that in a constant-speed pitch-controlled blade optimum power production can be achieved by twisting the inner blade toward feather while twisting the outer blade toward stall. Lobits (in 1996) [41] and Lobitz (in 2003) [25] consider both twist toward stall and feather. They report a 5-10% increase in annual energy from a maximum 2° twist toward stall. At the same time they report a substantial increase in fatigue damage. Rotor radius is increased to keep the same power

capacity. They report less fatigue loads with twist toward feather while a slight reduction in power [25]. By discussing optimal pre-twist in blades, Cappuzi [30] states that elastic twist can be employed to bring section twist angles closer to their optimal design value. He states pre-twist is not optimal but is a suitable compromise over all operating conditions.

Bend Twist Coupling can be introduced to a structure through material and geometry, as illustrated in Figure 7. In material bend twist coupling, which has been the focus among researchers in this area, composite lay-ups are employed to relate bending moment in a blade to the twist of its cross section. Biased fibers that are not in line with the structure's principle axis are key to creating this material property, illustrated in Figure 8. Off axis fibers oriented at 20° are shown to create optimum bend twist coupling [42]. Material, however, is not the only way BTC can be created. The geometry of the blade can also create BTC. An example of this is a swept blade, illustrated in Figure 9. In a curved design, the load applied on the parts off the pitch axis, creates pitching torque which results in an elastic twist [43]. Tests on full scale Sweep-Twist Adaptive Rotor (STAR) show a reduction in operating loads allowing for larger blades [29, 44]. A 12% increase in energy capture is reported by increasing the diameter by 10% while keeping the loads at the same level [29, 44]. A novel design by Capuzzi [31, 32] employs both material and geometry BTC for better results.

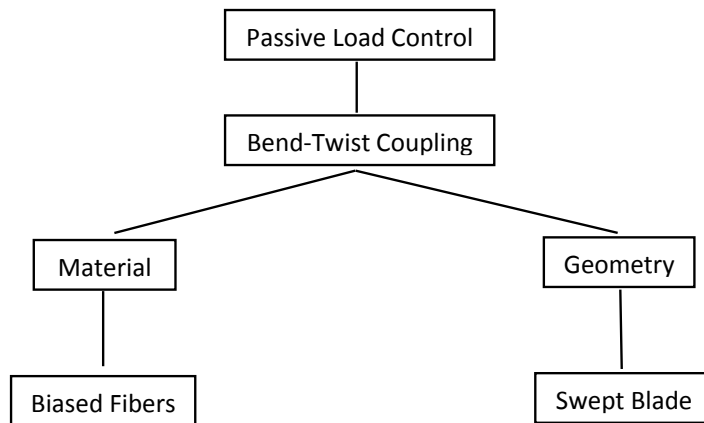


Figure 7. Variations of Bend Twist Coupling

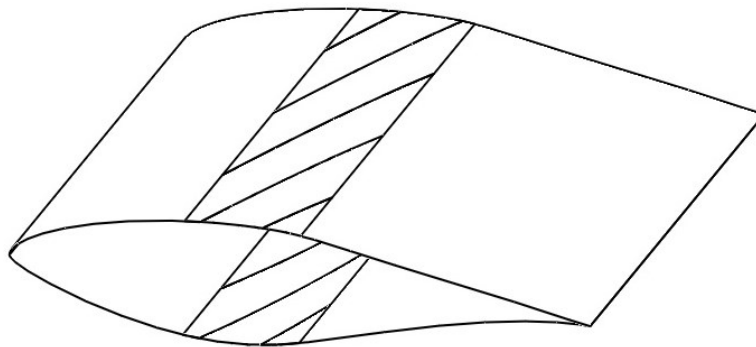


Figure 8. Biased fibers

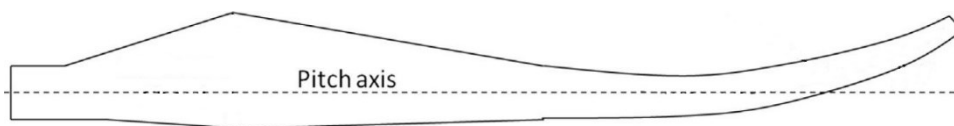


Figure 9. Swept blade planform [45]

Wind blades are designed such that they work the best at their rated TSR. This optimum TSR can be achieved in variable speed rotors by adjusting rotor speed (Ω) according to wind speed. However, in constant speed rotors, TSR will be different from its rated value at wind speeds other than the rated wind speed. As a result, the turbine will produce less power than

its rated power when the wind speed changes. The blade function can be improved if the angle of attack of the blade could adapt to the new wind condition. This can be achieved if the blade could passively twist to adjust the angle of attack. The Blade Element Theory (BET) can be used to find the optimum angle of attack for each blade section.

1.5 Objectives and Overview of Thesis

The main objective of this study is to employ a specific type of spar to aeroelastically tailor wind turbine blades. The potential of using an angle spar to provide BTC in wind turbines will be studied. By employing an angle beam spar in the blades we can benefit from its Bend Twist Coupling to passively control loads on the blade. This can be done with the purpose of power optimization or load alleviation. In this thesis, power optimization is being considered and load alleviation capacities of the spar are deferred to future studies. The blade planform is modified to a swept blade to benefit from its BTC property.

In Chapter 2 (Formulation), BEMT is implemented on NREL Phase VI blade to predict power output of the turbine at different wind speeds. The predictions are verified with experimental data. Optimization is done on the power to find optimal pitch angles and corresponding optimal elastic twists for each blade section at different wind speeds. Also, different spar types are discussed in the chapter, as well as fluid-structure interaction (FSI). In Chapter 3 (Results and Discussion) elastic twist potential of an L beam is studied and the L spar is designed to be incorporated into the blade. Finite element model of the blade and the CFD model are discussed. Verification of the CFD mesh and the mesh independence study are presented in this chapter. A comparison between 1-way and 2-way FSI is performed and presented. Induced elastic twist predicted from 1-way FSI analysis is presented for variations of

the spar at different wind speeds. A modified swept blade planform is proposed and FSI analysis is conducted for different bend depths. The power output change due to elastic twist from the swept blade model with L spar is predicted.

2 Formulation of bend-twist coupling

2.1 Blade Element Momentum Theory and Optimization

In horizontal axis wind turbines (HAWT) lift force creates torque around the rotor axis and rotates the low speed shaft. The relative wind speed passing over the blade consists of two components perpendicular to each other: real wind velocity, U_∞ , and blade rotation speed, Ωr . Placing a rotating turbine in wind causes the wind to change speed and pattern. As wind approaches the blade it expands and its speed reduces (see Figure 10). At the same time, because of the blade rotation, the wind will find a radial speed component that rotates in the opposite direction with respect to the blade rotation direction (see Figure 11). The reduction in incoming wind speed is represented by the axial flow induction factor, a , shown in Figure 3a. Similarly, the rotation of air on the blade plane of rotation is represented by the tangential flow induction factor, a' . The factors a and a' are later calculated using equations derived from the Blade Element Momentum Theory.

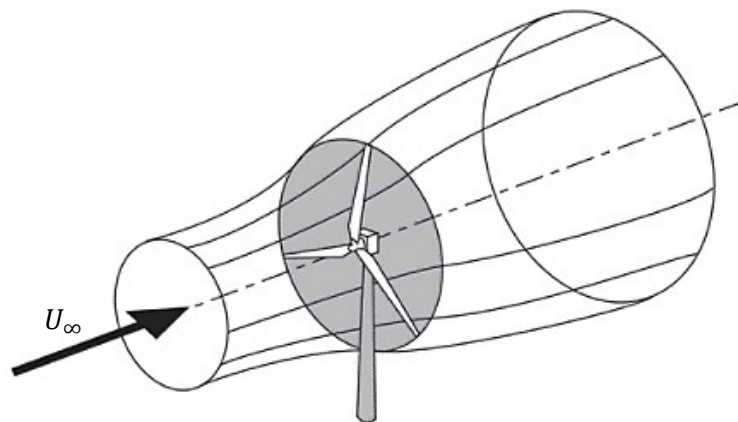


Figure 10. Streamlines passing through a wind turbine [5]

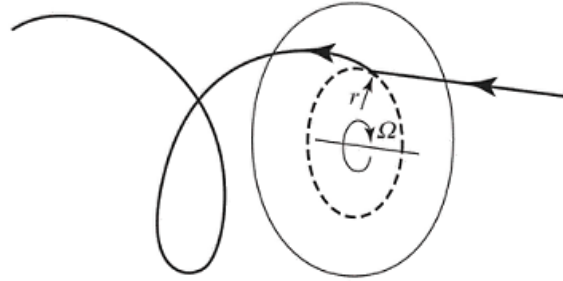


Figure 11. The trajectory of an air particle passing through the rotor disc [5]

To better illustrate the aerodynamics of a wind turbine, a figure of a 3 bladed working wind turbine and the related angles are presented in Figure 12. Angle θ_p is the section pitch angle and α is the section's angle of attack. From Figure 12, it can be understood that when wind speed rises, α will increase. Also, for blade sections closer to the tip, the velocity vector $r\vec{\Omega}$ is greater resulting in a relative wind velocity vector, \vec{w} , tilted closer to the plane of blade rotation.

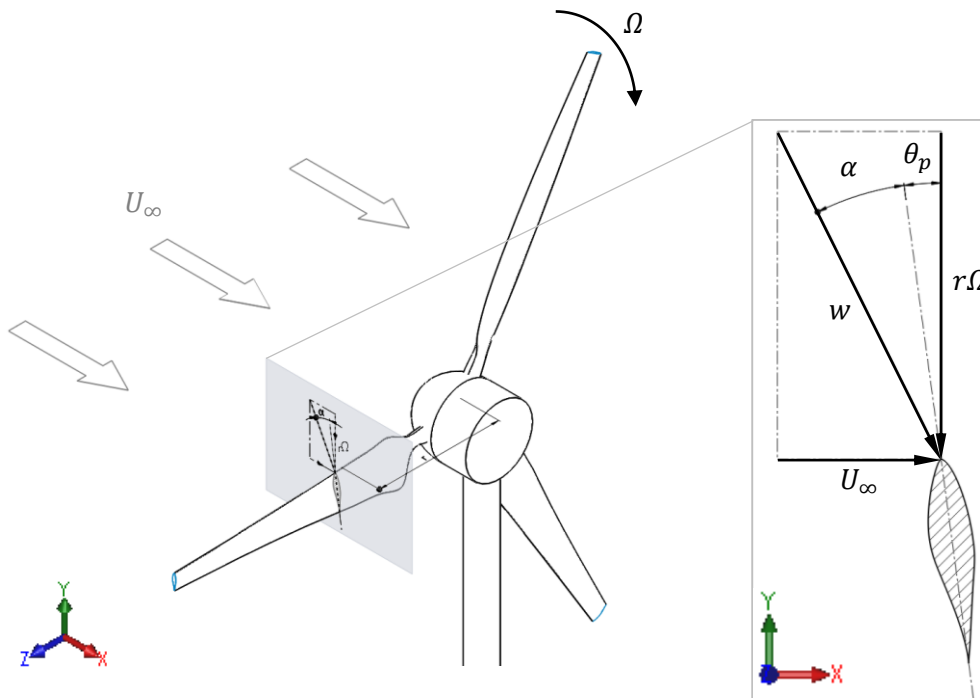


Figure 12. Wind turbine and blade section

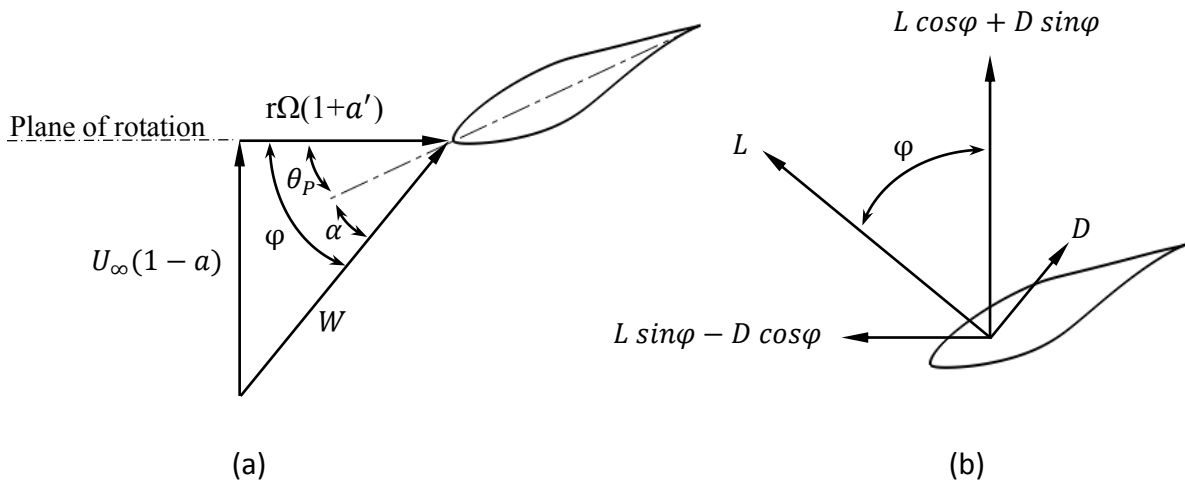


Figure 13. Aerodynamics of a typical wind turbine for (a) blade section velocities (b) and forces
(modified from [5])

As illustrated in Figure 13a, relative wind speed makes an angle φ with the blade plane of rotation. Lift and drag forces are parallel and perpendicular to the relative wind speed direction, respectively. The section force component $\delta F = L \sin \varphi - D \cos \varphi$ that creates torque around the rotor axis is shown in Figure 13b. Lift and drag forces can be obtained from Equation (2.1) and Equation (2.2) where C_l is the lift coefficient, C_d is the drag coefficient, L is the lift force, D is the drag force, ρ is the air density, W is the relative wind velocity, and A is the section area.

$$C_l = \frac{2 L}{\rho W^2 A} \quad (2.1)$$

$$C_d = \frac{2 D}{\rho W^2 A} \quad (2.2)$$

Substituting L and D into force component δF , for a section of blade provides

$$\delta F = \frac{1}{2} \rho W^2 \delta A (C_l \sin \varphi - C_d \cos \varphi) \quad (2.3)$$

The torque created from a section of the blade in distance r from the rotor axis is

$$\delta T = r \times \delta F \quad (2.4)$$

Substituting Equation (2.3) into Equation (2.4) gives an equation for a blade section torque

$$\delta T = \frac{1}{2} \rho W^2 \delta A (C_l \sin \varphi - C_d \cos \varphi) r \quad (2.5)$$

From Figure 13.a the magnitude of relative wind velocity can be calculated by

$$W = \sqrt{U_\infty^2 (1 - a)^2 + r^2 \Omega^2 (1 + a')^2} \quad (2.6)$$

Also,

$$\sin \varphi = \frac{U_\infty (1 - a)}{W} \quad (2.7)$$

$$\cos \varphi = \frac{r \Omega (1 + a')}{W} \quad (2.8)$$

$$\varphi = \tan^{-1} \left(\frac{1 - a}{(1 + a') \lambda_r} \right) \quad (2.9)$$

where λ_r is the section tip speed ratio and is defined as

$$\lambda_r = \frac{r \Omega}{U_\infty} \quad (2.10)$$

Substituting (2.7) and (2.8) into (2.5) provides

$$\delta T = \frac{1}{2} \rho W^2 \delta A \left(C_l \frac{U_\infty (1 - a)}{W} - C_d \frac{r \Omega (1 + a')}{W} \right) r \quad (2.11)$$

Power is the product of torque by angular velocity:

$$\delta P = \delta T \times \Omega \quad (2.12)$$

By substituting Equation (2.11) into Equation (2.12) an equation for the power of a section of the blade with the area of δA is developed:

$$\delta_P = \frac{1}{2} \rho W^2 \delta A \left(C_l \frac{U_\infty(1-a)}{W} - C_d \frac{r\Omega(1+a')}{W} \right) r\Omega \quad (2.13)$$

Power of the rotor now can be calculated by integrating δ_P over the span of the blade for both blades.

$$P = B \int_{r_0}^R \delta_P \quad (2.14)$$

where B is the number of blades.

Induction factors a and a' must be calculated before the power Equation (2.14) can be integrated. The Blade Element Momentum Theory is used to derive equations to solve for induction factors. Equations (2.15) and (2.16) are given from the BEM theory:

$$a' = \frac{1}{\frac{4 \cos \varphi}{\sigma' c_l} - 1} \quad (2.15)$$

$$a = \frac{a' \lambda_r}{\tan \varphi} \quad (2.16)$$

where, σ' is the Chord Solidity which is a measure of how much the blade chord covers the sweep circumference of the blade at a given radius.

$$\sigma' = \frac{Bc}{2\pi r} \quad (2.17)$$

Equations 2.15 and 2.16 are solved iteratively using the following steps. Initial values of $a' = a = 0$ are inserted into Equation (2.9) to get φ . Angle of attack then can be calculated from $\alpha = \varphi - \theta_p$. The corresponding Lift coefficient C_l is interpolated from a graph of C_l versus α . The new a' and a are calculated from Equations (2.15) and (2.16). This process is completed for the new a' and a and repeats until convergence.

These steps have to be conducted for each blade section as c , θ_p , λ_r and φ are all functions of r . From a and a' , Equation (2.13) can be integrated numerically to calculate the power output. A code is developed in MATLAB™ to do the calculations. Induction factors a and a' are presented in Figure 14. The estimated power output for different wind speeds are presented in Figure 15.

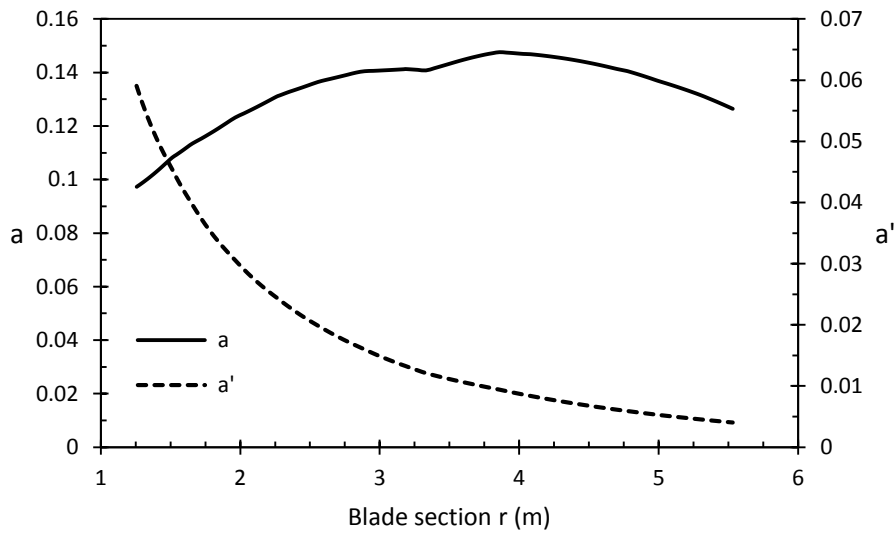


Figure 14. Induction factors at wind speed $U_\infty = 8 \text{ m/s}$

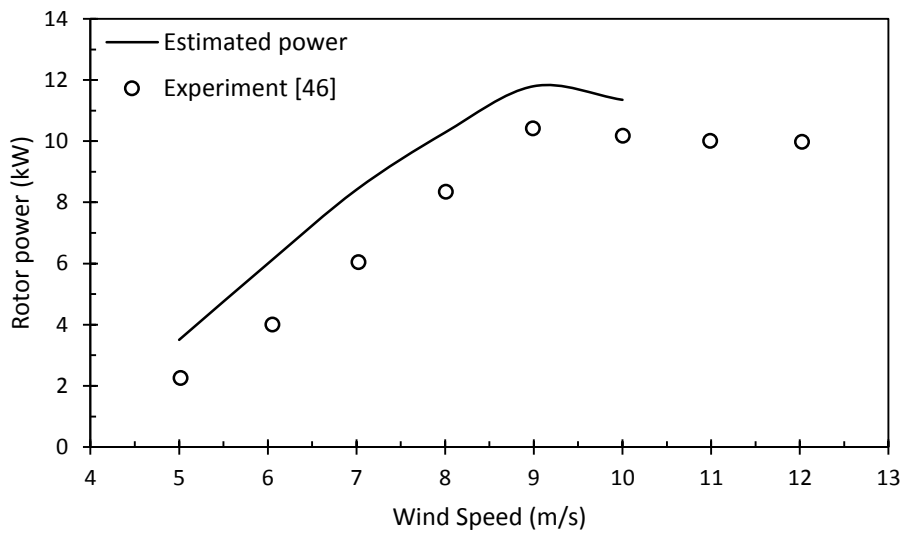


Figure 15. Rotor power versus wind speed

Rotor power results for speeds below rated are presented and verified with experimental tests done on a full scale NREL Phase VI rotor at NASA Ames Research Center [46]. As illustrated in Figure 15, the code overestimates power output by an average of 20%. This could be due to not considering tip / hub losses and stall delay. The results show good agreement and a similar trend with the experimental data. The blade goes into stall when it reaches its rated power of 10 kW at 10 m/s wind speed.

An optimization algorithm was incorporated in the code to find the optimized angle of attack for each blade section of the NREL Phase VI turbine. The algorithm works by trying different angles of attacks on each blade section to find the one that maximizes the section torque (δ_T), and consequently the section power (δ_P). In the analysis, 80 angles of attack were tested, between 0° and 40° , at each blade section for each wind speed ranging 5m/s to 10 m/s. Blade span was divided into 100 sections each of 4.275 cm. The code completed 48,000 loops to find the optimized angle of attack and the corresponding optimized power output for each wind speed. The results are presented in Figure 16. As the NREL Phase VI is a stall controlled blade, it is designed to stall and shed power after rated speed, for this reason, the code was not run for speeds higher than 10 m/s.

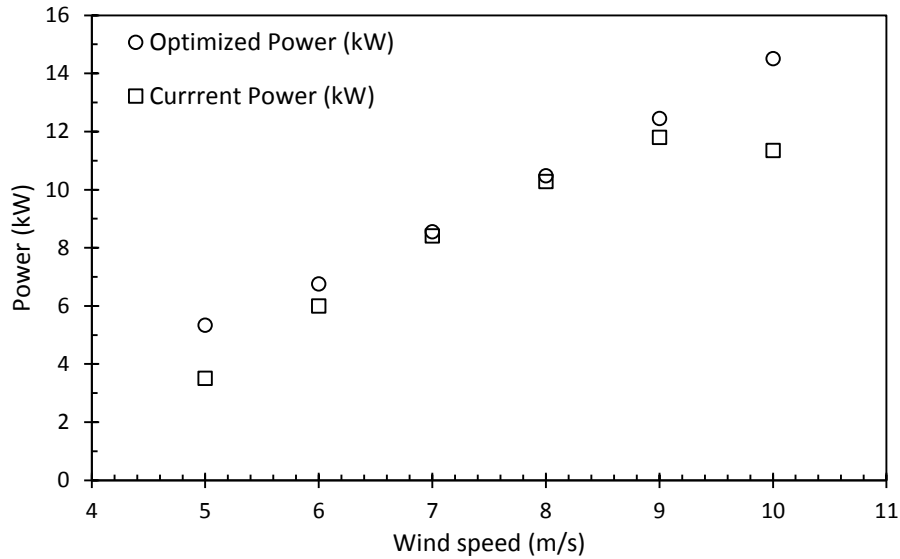


Figure 16. Optimized power

NREL Phase VI is a two-bladed stall-controlled wind turbine designed and developed by NREL. The blade was tested at full scale at the NASA Ames Research Center wind tunnel (24.4 × 36.6 m). The study is one of a few full scale tests that focus on 3D effects of flow on a working turbine. As the design process of wind turbines relies mainly on data from 2D tests on airfoils, this experiment provided insights on the 3D effects on a running full scale turbine in wind tunnel. The blade chord and twist are presented in Figure 17, Figure 18 and Table 1.

The potential for increased power output is mainly in lower wind speeds and around the rated speed, however, at the rated speed, the blades are designed to go in stall to control and limit power output. As a result, any power increase after the blade has reached its rated power is not favorable. From 6.5 m/s to 8.5 m/s, the power output is almost equal to its optimized value. This shows that the twist designed in the blade provides the optimum angle of attack for all blade sections in this narrow wind speed range.

The optimal pitch angles needed for optimized power for each wind speed are shown in Figure 19. These curves compare against the already applied blade pitch angle that is 3° and constant along the blade. At lower wind speeds the lines are rather flat and indicate that a constant blade pitch can work, however, at higher speeds, the lines show larger pitch closer to the root and smaller pitch closer to the tip. Compared to 3° constant pitch, the curves show the induced elastic twist must be nose down for higher wind speeds. Nose down twist, which is also called twist to feather, has been mentioned in the literature for the purpose of power optimization.

NREL Phase VI Rotor characteristics

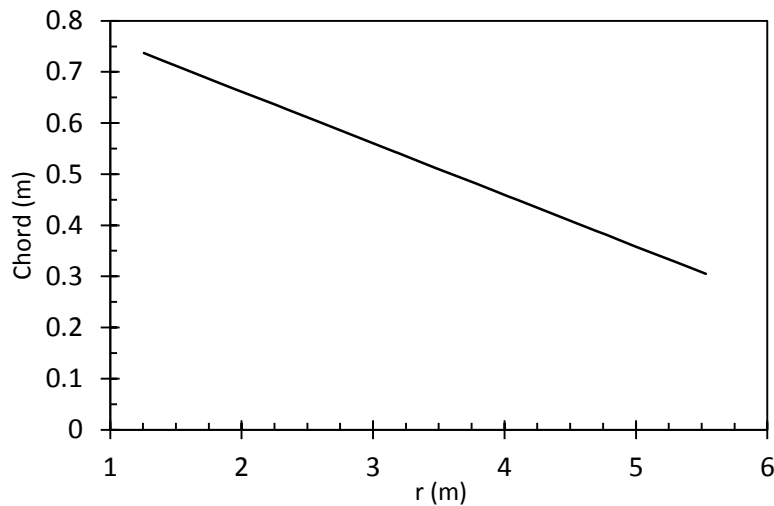


Figure 17. Chord distribution [47]

Table 1. Blade chord and twist distribution [47]

r (m)	Chord (m)	Twist (°)
1.257*	0.737	20.04
1.343	0.728	18.074
1.510	0.711	14.292
1.648	0.697	11.909
1.952	0.666	7.979
2.257	0.636	5.308
2.343	0.627	4.715
2.562	0.605	3.425
2.867	0.574	2.083
3.172	0.543	1.150
3.185	0.542	1.115
3.476	0.512	0.494
3.781	0.482	-0.015
4.023	0.457	-0.381
4.086	0.451	-0.475
4.391	0.420	-0.920
4.696	0.389	-1.352
4.780	0.381	-1.469
5.000	0.358	-1.775
5.305	0.328	-2.191
5.532	0.305	-2.500

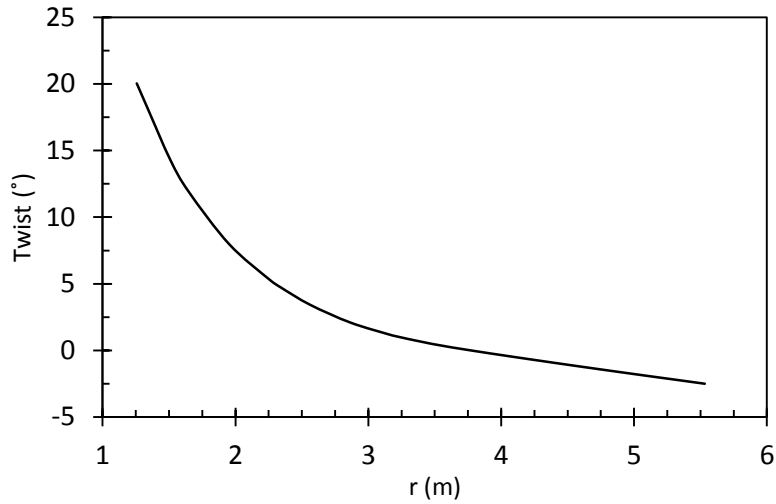


Figure 18. Twist angle distribution [47]

*Transition NREL S809 airfoil completes at the section 1.257 m from the rotor axis, as a result all of the calculations and modeling of the blade take this point as the root of the blade

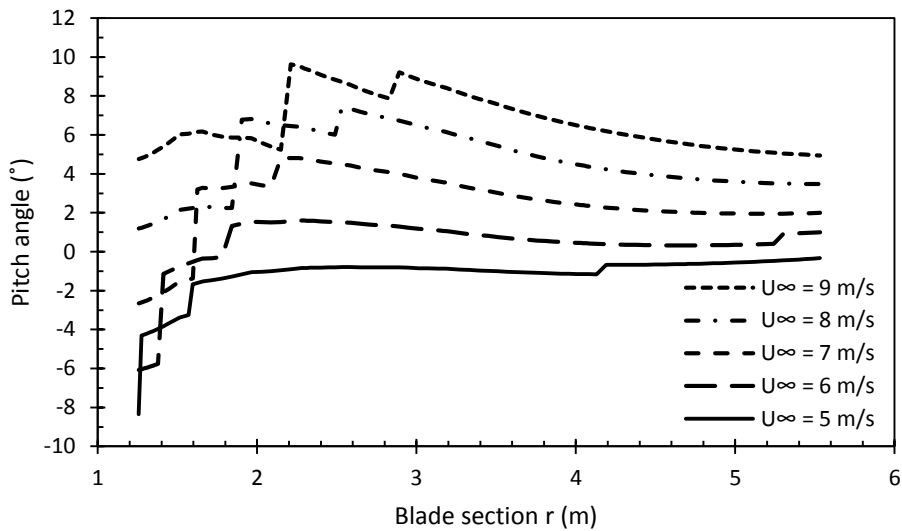


Figure 19. Optimal pitch angles for maximum power output at various wind speeds

The desired induced twist for 8 m/s wind speed is 3.5° at a 30% span and decreases to 0.6° at the tip. Figure 20 shows the optimal pitch angle only for $U_{\infty} = 8$ m/s. For the majority of the blade span, the optimal pitch angle stays higher than the constant blade pitch angle, $\theta_{P,0} =$

3°. This indicates elastic induced twist must be nose down for all blade sections which makes this concept feasible.

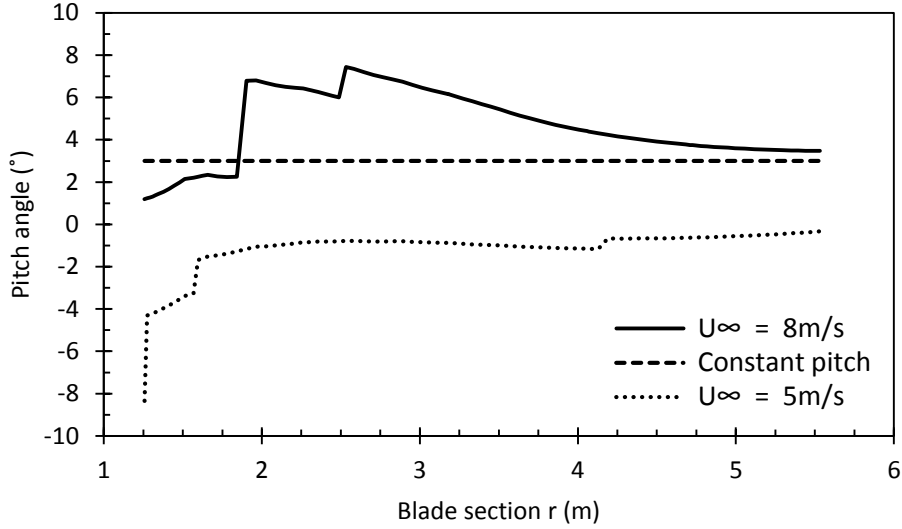


Figure 20. Optimal pitch angle for maximum power output at $U_\infty = 8 \text{ m/s}$ and $U_\infty = 5 \text{ m/s}$

In the conventional blade design process, the section pitch angle is the summation of the blade pitch angle and section twist angle. Figure 21 is a sketch of the airfoil section and related angles.

$$\theta_P = \theta_{p,0} + \theta_T \quad (2.18)$$

where for each section of the blade, θ_P is the section pitch angle, $\theta_{p,0}$ is the blade pitch angle (constant for all sections) and θ_T is the twist angle. In an adaptive design, however, an extra term for elastic twist is introduced so the equation becomes:

$$\theta_P = \theta_{p,0} + \theta_T + \theta_e \quad (2.19)$$

where θ_e is the induced elastic twist.

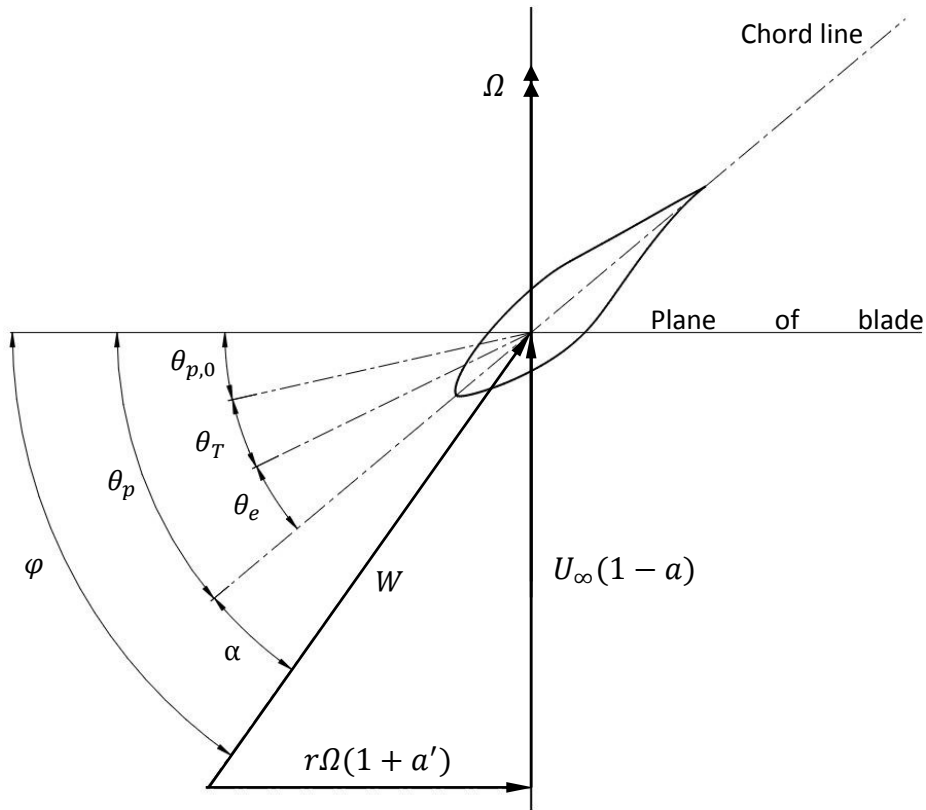


Figure 21. Blade section forces and angles

The elastic twist, θ_e , is a new variable introduced to the pitch angle equation. This variable adds an extra term to the equation and makes it theoretically possible to achieve the optimal pitch angle distribution presented in Figure 10. Figure 22 is a plot of induced elastic twist, θ_e for $U_\infty = 8$ m/s. The desired induced twist for 8 m/s wind speed is a 3.5° at 30% span and decreases to a 0.6° at the tip. Although the exact optimal pitch angle distributions cannot be achieved because of their non-monotonic behavior, the target curves can be developed that closely resemble the same pattern. Adding the elastic twist angle to a constant blade pitch angle makes it possible to achieve the target section pitch angles.

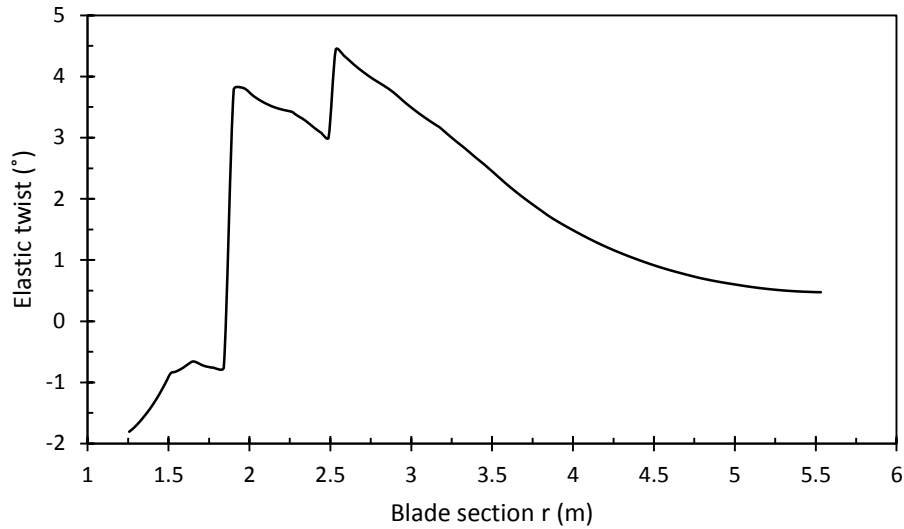


Figure 22. Desired elastic twist for $U_{\infty} = 8 \text{ m/s}$

The desired elastic twist curve in Figure 22 shows two abrupt spikes, and then a reduction creating two local maximums in the curve. This is due to two sudden reductions in optimal angle of attack at sections $r = 1.84 \text{ m}$ ($r/R = 33\%$) and $r = 2.5 \text{ m}$ ($r/R = 45\%$) (Figure 23). The sudden reductions happen because of the nature of the term, $(C_l \sin \varphi - C_d \cos \varphi)$, which is the portion of the differential torque equation of a section of the blade that is being optimized (Equation 2.5). Figure 24 compares plots of the term $(C_l \sin \varphi - C_d \cos \varphi)$ for two sections of the blade at $r/R = 30\%$ and $r/R = 50\%$. The maximum points on these curves correspond to the optimal torque and power, as well as the corresponding α is the optimal angle of attack for that section of the blade. As it is illustrated, each curve has two local maximums and the curves pivot from one section to another making the global maximum to jump from the right side to the left side rather than making a smooth transition. For instance, as marked on Figure 24, the global maximum jumps from 14.5° at $r/R = 30\%$ to 8.5° at $r/R = 50\%$. Although the global maximums are used in the optimization routine, the local maximums are almost of the same magnitude as the curve is almost flat at the top part.

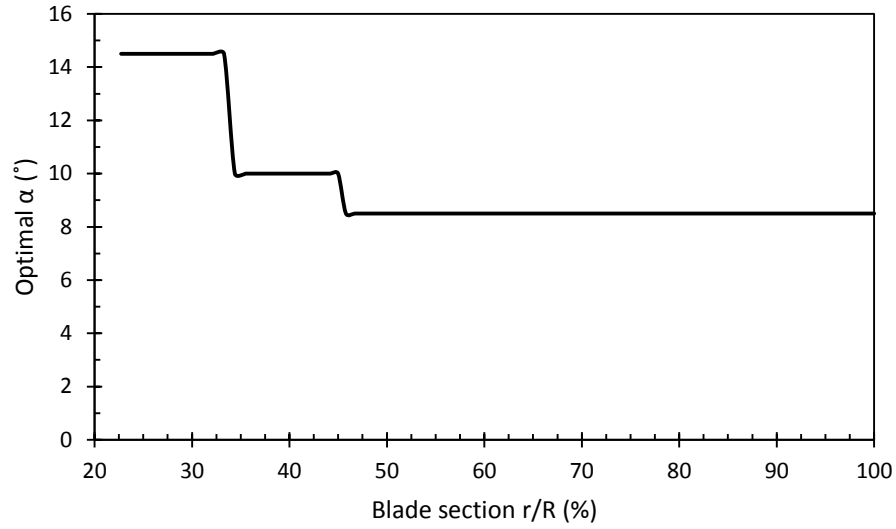


Figure 23. Optimal angle of attack at $U_\infty = 8 \text{ m/s}$

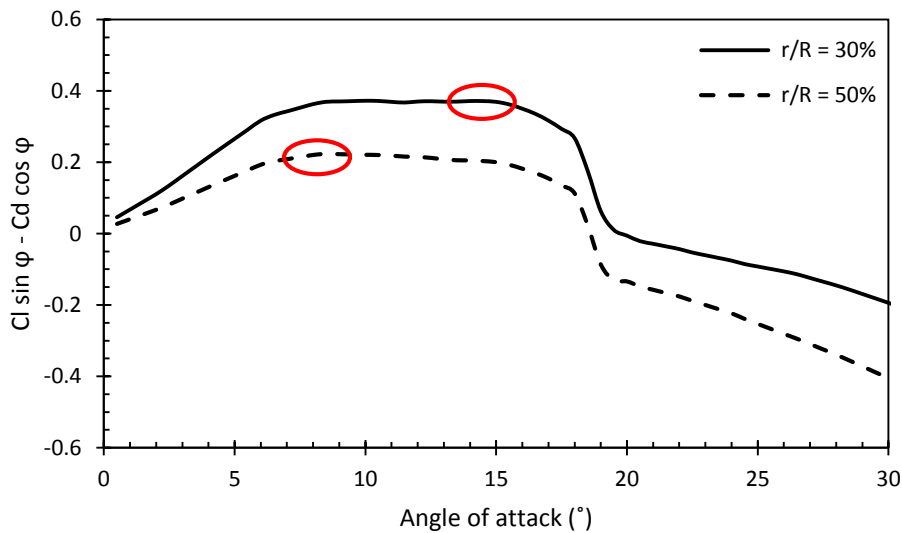


Figure 24. Finding optimized angle of attack

2.2 Spar Selection

Figure 25 illustrates a typical modern wind turbine blade with pre-twist and taper. Spar is a blade component that supports a large portion of the induced loading. As illustrated in Figure 26, spars have a variety of different designs. Spar cap mainly bears the bending loads whereas shear web stabilizes the spar caps under shear loads [48]. Different designs of spars

have different static structural response under loads. The structural response can be tailored for improving the performance of the wind turbine. Since the main load-bearing component of the blade is spar, the structural response of the spar is assumed to be the blade's structural response [48].

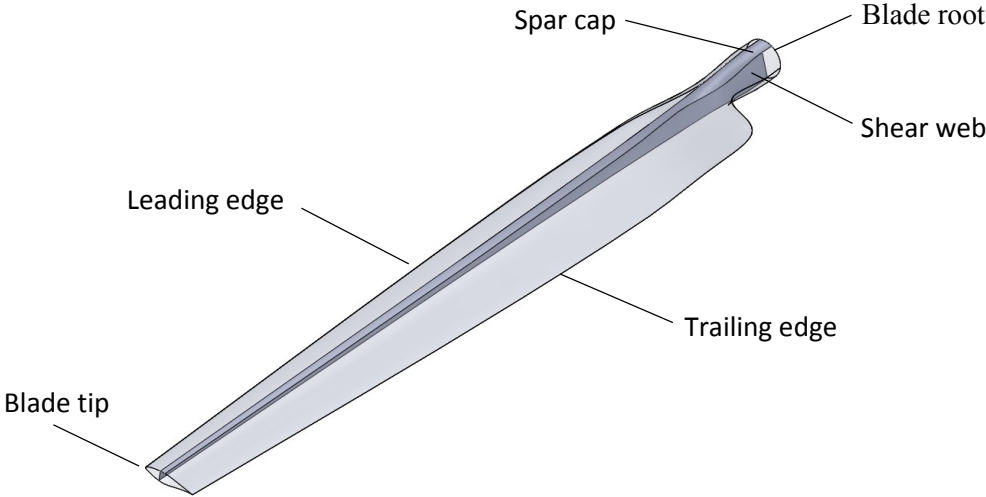


Figure 25. Wind turbine blade components

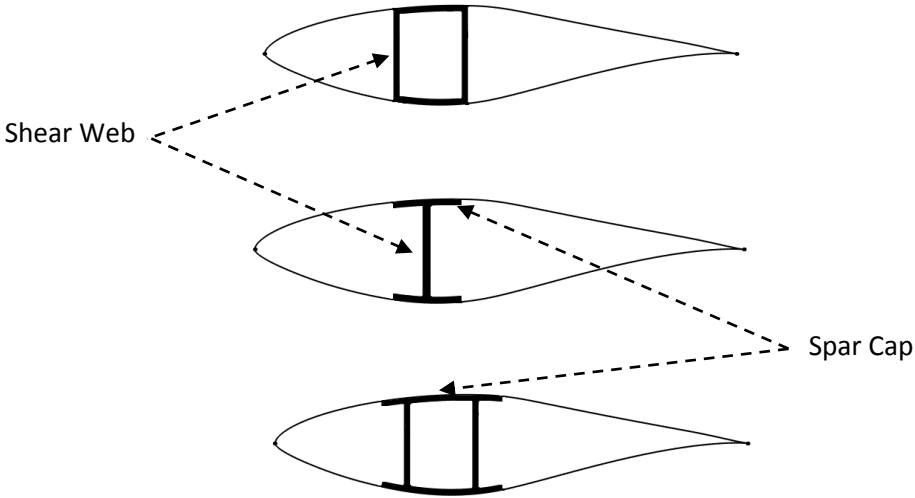


Figure 26. Different Spar designs.

Spars can have open or closed sections, as shown in Figure 26. Closed sections allow for the formation of a cell shear flow circuit which takes up the internal torque and resists torsion much more effectively [49]. The shear flow circuits are internal forces per unit length tangential to the wall (Figure 27). An uninterrupted circuit for a shear flow cannot be established in an open section.

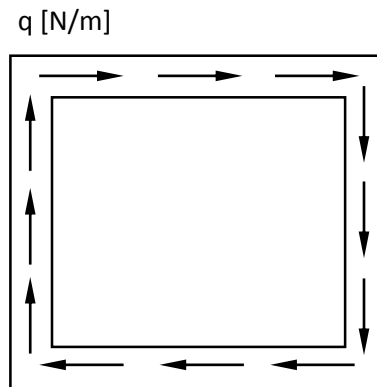


Figure 27. Shear flow in a box section

An open section will twist more than a closed section with the same load and dimensions. This is because a shear flow circuit can develop in a closed section and resist applied torque. Figure 28 shows torque application on a closed and open rectangular section with the same dimensions. Using statics analysis, it can be shown that the twist of the open section is orders of magnitudes greater than that of the closed section. Therefore, an open section for the spar can be more effective in geometry-based BTC.

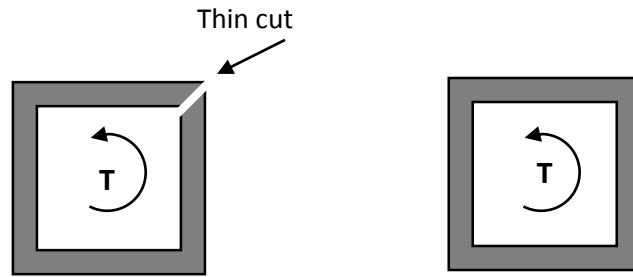


Figure 28. Closed and open rectangular sections

Each cross section has a shear center. Shear center is a point around which the lateral force creates zero torque. A lateral load that does not pass through the shear center creates torque, which causes the section to twist. The magnitude of torque is proportional to force, F , and lever arm, d , which is the perpendicular distance from the load to the shear center, (Figure 29). The greater amount of torque applied on a beam, the more the section twists. Therefore, F and d are variables that can be utilized to tailor the twist of a section. The aerodynamic force applied on a spar cross section is a function of turbine operating conditions and design parameters that are selected for a variety of design purposes. However, d is a variable that is less restricted and can be modified for our purpose of bend twist coupling.

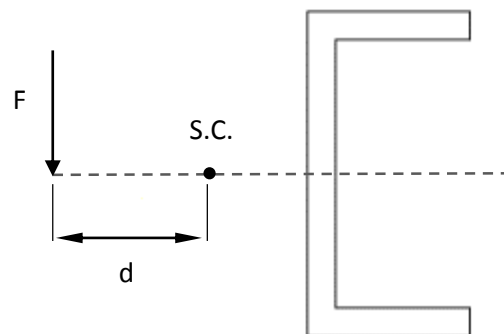


Figure 29. Channel section

An angle section is shown in Figure 30. The shear center of the section is located at the corner, providing more perpendicular distance for twist coupling compared to a channel section (Figure 29). As illustrated in Figure 27, the shear center is located on the axis far from the shear web, thus reducing lever arm and induced torque.

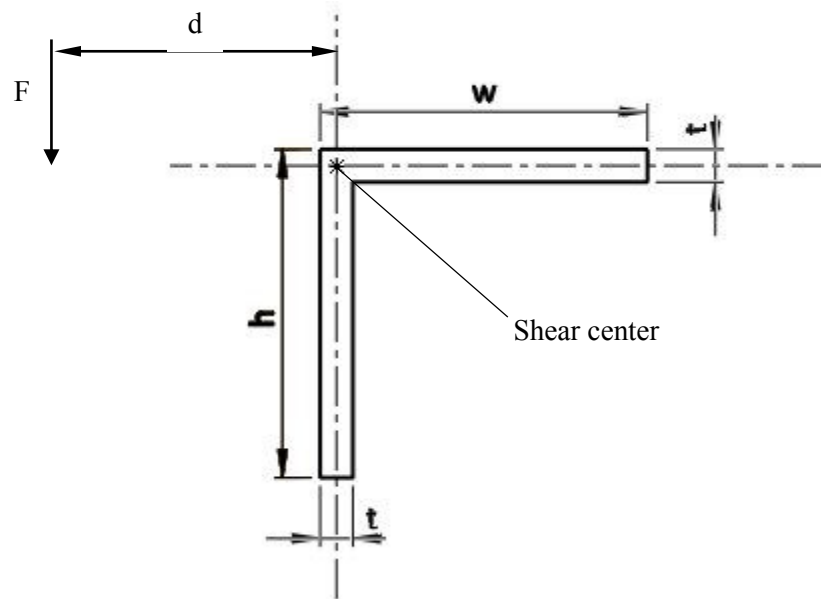


Figure 30. Schematic of spar section

Aerodynamic forces applied on an airfoil can be represented by lift and drag forces. Distributed pressure on airfoil is integrated and then resolved to two components perpendicular and parallel to the vector of relative wind velocity, which are lift and drag, respectively. The center of pressure is a point usually on the chord line through which the resultant force passes without producing torque, as illustrated in Figure 31. As a result, this point is a necessary coordinate in airfoil force analysis. Since lift and drag change with angle of attack (α), center of pressure location is also a function of α . To conduct a statics analysis on the blade section, it is important to locate this point which can be done with approximate

methods or CFD analysis. In this thesis, the center of pressure for the airfoil is located using numerical methods and is presented in Chapter 3.3.

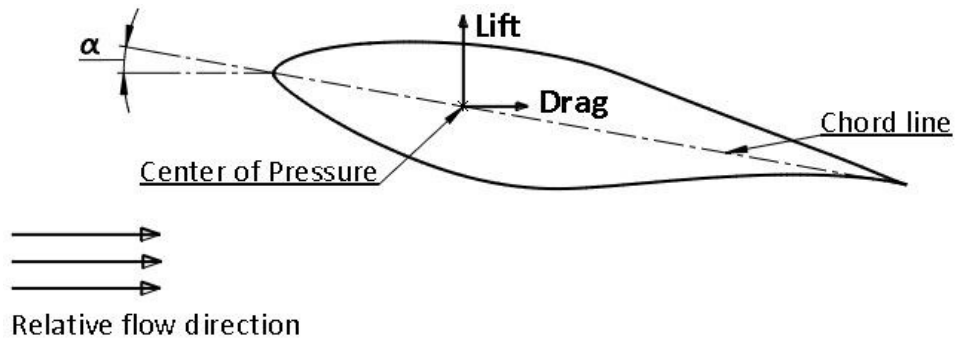


Figure 31. Lift and drag forces at the center of pressure

A free body diagram (FBD) of the blade section is illustrated in Figure 32. The perpendicular distance between the center of pressure of the airfoil and the shear center of the spar is denoted by S . Based on the analysis presented in Section 2.1 (desired induced elastic twist), incorporating the angle beam spar in the airfoil section must be such that it maximizes the nose down torque on the beam. Torque is product of force and distance, thus, by increasing the distance S , torque will be increased. Although drag force also creates nose down torque, this torque is usually neglected in calculations because drag is much smaller than lift. For the lift and drag to produce a nose down moment, the center of pressure must be placed on the right hand side of the spar shear center. Figure 32 illustrates that lift and drag produce positive moments (nose down) around the shear center.

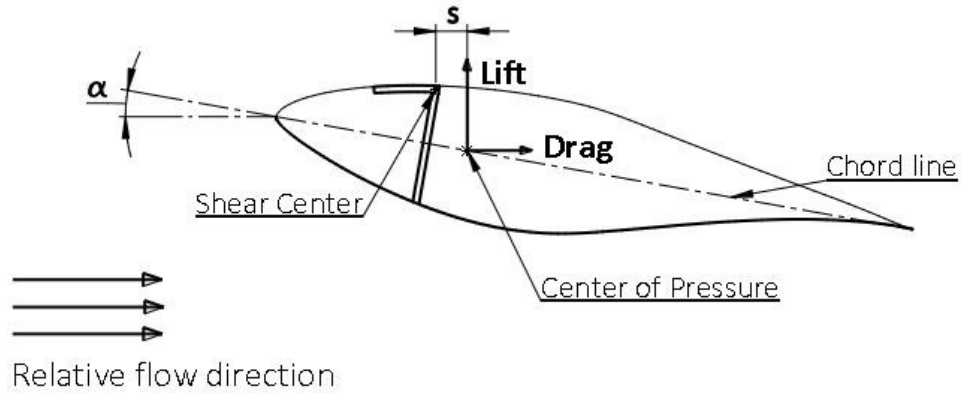


Figure 32. Blade cross section free body diagram

The angle section can be placed inside the airfoil in two potential orientations. The spar can be either facing the trailing edge (Figure 33.a) or leading edge (Figure 33.b). The selection of orientation is based on a simple finite element analysis that compares the elastic twist of both cases in the same conditions. The orientation with the greatest elastic twist will be selected. Geometric constraints from the airfoil shape will also limit where the spar is located.

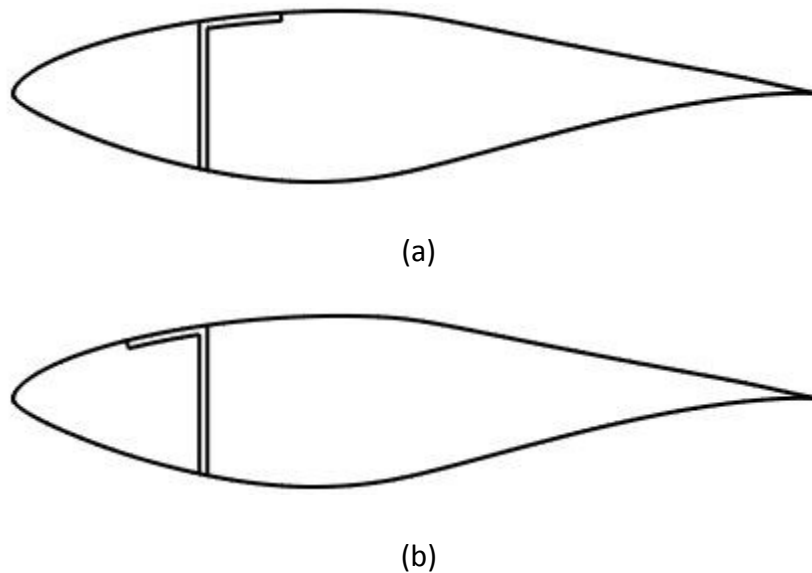


Figure 33. Spar orientations with the cap facing (a) right and (b) left

2.3 Fluid Structure Interaction

Fluid-structure interaction in wind turbines is a complex phenomenon. The blade cross section (airfoil) changes the direction of air passing over it causing a pressure difference between the both sides of the airfoil. This pressure difference results in lift and drag forces under which the blade deforms. Analytical solutions of fluid-structure interaction are very complex and sometimes impossible because of the coupled nature of its governing equations. However, thanks to advances in computational power, it is possible to numerically study complex FSI models. Experimental tests can also be conducted to study interaction between fluids and solids.

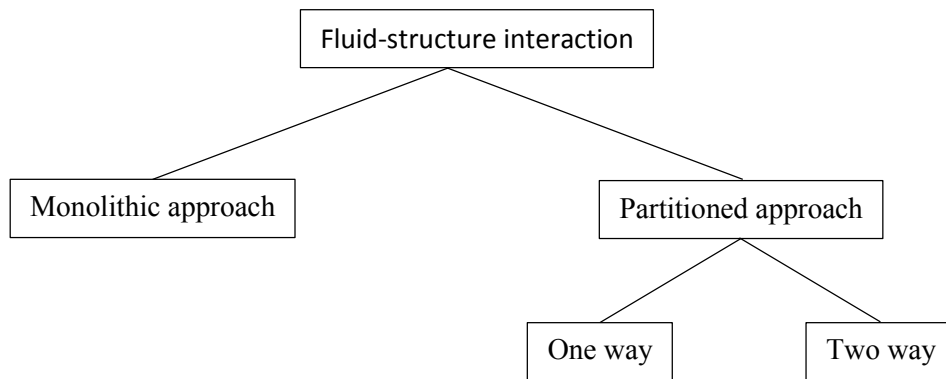


Figure 34. Numerical solution methods for Fluid Solid Interaction problems

Numerical methods to solve FSI problems are classified as monolithic approach and partitioned approach. In monolithic approach, the equations for solid and fluid domains are in a single coupled system of equations and are solved simultaneously using a unified solver. This approach provides strong coupling between domains, guarantees conservation of energy on the interface and is potentially more accurate. However, the need for development of specialized codes and high storage resource needed are disadvantages of this method. Partitioned approach uses already available fluid and structural codes to solve each domain

separately and through an iterative approach, satisfies interface conditions. The ability to use conventional fluid and structure codes with minimal modification is the main advantage of partitioned methods. However, lack of convergence is more likely with this method [50, 51].

A partitioned approach analysis can be conducted in one-way or two-way (Figure 35) [52]. As illustrated in Figure 35, in a one-way analysis forces from fluid are transferred to the structure as loading and the analysis continues in structure side. The fluid side will not be updated with deformations in the structure. This obviously is a simplification as in some FSI problems, the structure deformation will modify the flow at the interface and this in turn will change the forces applied on the structure from the fluid. This is called a weak coupling between fluid and solid and can be an acceptable simplification if the deformations in structure are negligible. In problems where structure deformation and its effect on the flow is considerable, two-way method is employed. In the two-way method, once deformations are calculated in solid side, they are passed to the fluid solver. The mesh is updated with the new interface location and the new fluid analysis is performed with the updated grid. Iterations will continue until displacements and forces on the interface converges. If a sufficient quantity of iterations are used in each time step, conservation of energy will be ensured and strong coupling will be achieved [53, 54].

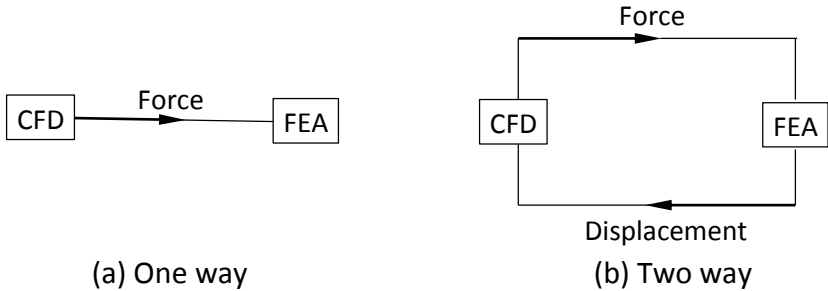


Figure 35. One way and two way FSI

As the interface is at a new location after each iteration, the mesh needs to be moved accordingly. Diffusion-based smoothing method, which is superior in handling rotational motion, is used to update the grid [55]. Mesh motion governing Equation (2.20) is solved numerically to find vector \vec{u} , which is mesh displacement velocity. The diffusion coefficient γ is used to control how the boundary motion affects the interior mesh motion [55]. The new location of each node then can be calculated using Equation (2.21).

$$\nabla \cdot (\gamma \nabla \vec{u}) = 0 \quad (2.20)$$

$$\vec{x}_{new} = \vec{x}_{old} + \vec{u} \Delta t \quad [55] \quad (2.21)$$

2.4 Measuring elastic twist

As the blade is pre-twisted and a pitch angle of 3° is applied, each section of the blade already has a pitch angle which has to be compared with that of the deformed blade. Figure 36 and Equations (2.22) and (2.23) illustrate the method to calculate induced elastic twist for each blade section.

$$\theta_p' = \text{Sin}^{-1} \left(\frac{y_{trailing\ edge} - y_{leading\ edge}}{C} \right) \quad (2.22)$$

$$\theta_e = \theta_p' - \theta_p \quad (2.23)$$

where θ_p' is the section pitch angle after deformation, θ_p is the undeformed section pitch angle, c is the chord length for each section of the blade.

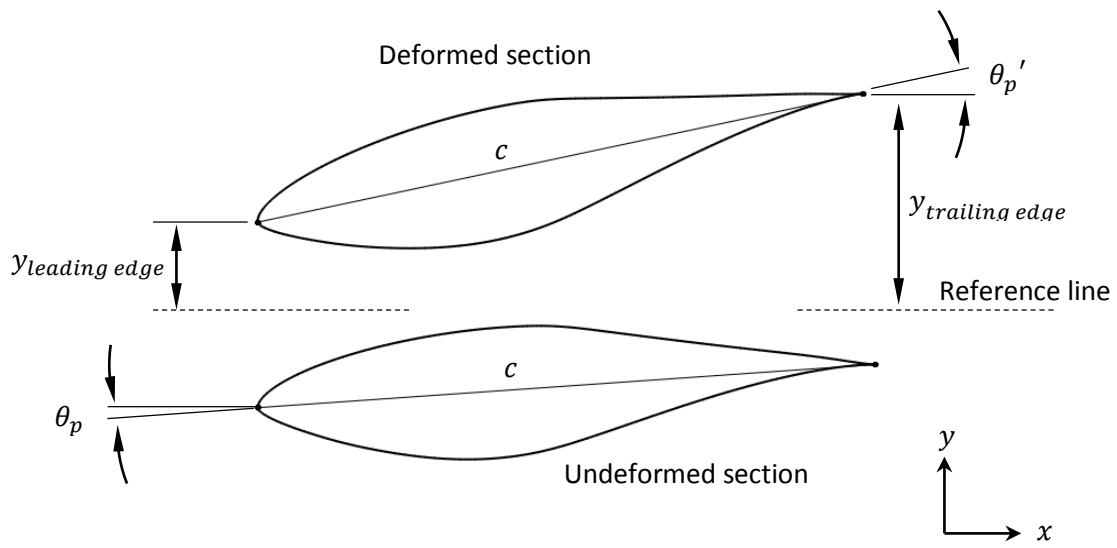


Figure 36. schematic of the blade section after and before deformation

3 Results and Discussion

3.1 Angle beam bend twist coupling potential

To investigate the magnitude of twist angle that can be expected from an angle section, a finite element analysis is performed. An angle beam was modeled and static structural analysis was conducted using Ansys Mechanical. The beam thickness and length are 10^{-2} m and 5.532 m respectively. Figure 37 shows the beam and applied loading. A fixed support boundary condition is applied at the end of the beam and a distributed load, ω , is applied at a distance d from the beam shear center, resembling aerodynamic loading of an airfoil. The load vector, $\vec{\omega} = 4.7 \hat{i} + 104.7 \hat{j}$ N, is the resultant force at wind speed $U = 14.6$ m/s and angle of attack $\alpha = 7^\circ$.

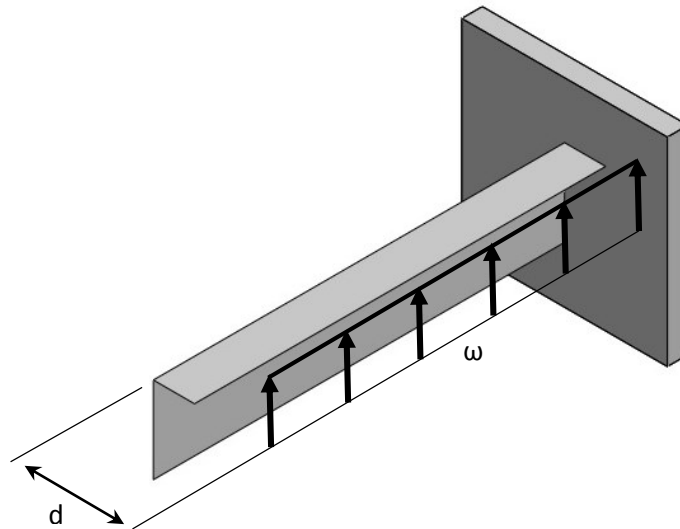


Figure 37. Angle beam

Shell181, which is a 4-node element, is used in the beam FE model. This element has 3 translational and 3 rotational degrees of freedom at each node making it suitable for analyzing thin shell structures [55]. In the FE model, there are 62,640 elements and 63,745 nodes. The

same (equivalent) material properties that are later used for the blade model are also used for the beam FE analysis. An elasticity modulus of $E = 1.56 \times 10^{10}$ Pa and Poisson's ratio of $\nu = 0.42$ are employed [56]. A mesh independence study is conducted on the model and the results are presented in Table 2.

Table 2. Finite element mesh independence study for angle beam

Quantity of Elements	max flapwise Y deformation (m)	max chordwise x deformation (m)
4,185	0.02029	0.01768
16,650	0.02035	0.01768
66,480	0.02039	0.01768

Twist angles of the beam tip for different values of d are presented in Table 3. An illustration of flapwise deformation is presented in Figure 38. Diagonal contours of flapwise displacement on the beam flange indicate the presence of twist in the beam. As presented in Table 3, considerable twist angles can be achieved even for lever arm distances as low as 0.1 m.

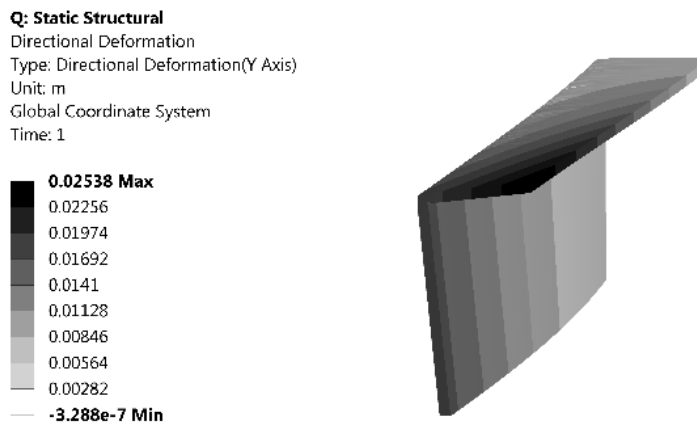


Figure 38. Angle section beam flapwise deformation

Table 3. Twist of the beam at the tip

d (m)	Elastic twist at the tip (°)	maximum flapwise deformation (m)
0.1	3.04	0.0202
0.15	4.55	0.0228
0.2	6.06	0.0257

3.2 Orientation of spar

A finite element model for an angle beam facing the leading edge is analyzed and the results are compared to the results presented in Section 3.1. Table 4 presents the elastic twist from both beams, showing that the models' elastic twist are almost the same in each loading case. As a result, geometric constraints were considered to select which orientation should be used. The orientation with the L section facing right was selected because it provides a broader cap on the sections of the airfoil which are more flat than curved.

Table 4. Elastic static structural response of angle beams

d (m) - Perpendicular distance from shear center, CS	Elastic twist at the tip (°)	
		
0.1	3.04	3.02
0.15	4.55	4.54
0.2	6.06	6.04

3.3 Locating NREL S809 airfoil center of pressure

A series of 2D steady state CFD analyses are conducted on an NREL S809 airfoil to locate its center of pressure. Angles from 2° to 17° are considered which is the range of α for all blade sections at the operational wind velocities. Table 5 presents the location of center of pressure measured in percent of chord length from the airfoil tip along the chord. In all of the models,

wind velocity and Reynolds number are 14.6 m/s and 1 million, respectively. A mesh independence study is conducted with three different mesh densities monitoring the lift coefficient and the center of pressure location. The results from the mesh independence study are presented in Table 6.

Table 5. Location of center of pressure

α (°)	C.P. (%C)
2	36.3
7	30
12	28.2
14	27.9
17	28.3

Table 6. Mesh independence study for 2D C-grid

Quantity of cells	Quantity of nodes around airfoil	Lift coefficient	C.P. (%Chord)
14,465	168	0.3123	36.36
39,105	300	0.3139	36.4
63,935	528	0.3134	36.35

3.4 2D CFD verification

As illustrated in Figure 39, a C-grid structural mesh is generated around the airfoil. The mesh consists of 63,935 cells and the first layer thickness is $10^{-3} m$. There are 528 nodes around the airfoil. Finite volume method is used to solve the governing equations of continuity and momentum. Equations (2.24) – (2.27) are governing equations for air flow with the following assumptions: 1 - the flow is steady state, 2 - the flow is incompressible, 3 - viscosity is constant. The turbulence model $k - \epsilon$ standard is used with standard wall functions. The lift and drag coefficients are monitored for convergence and the iterations are carried on until all

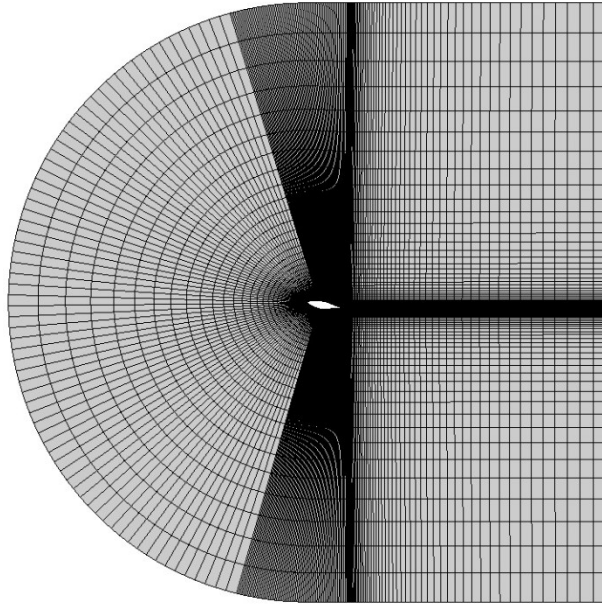
residuals drop below 2×10^{-5} . To verify the 2D CFD results, pressure distribution around the airfoil is shown in Figure 40 [57]. A Dense mesh around the blade is used. The plot shows good agreement between numerical and experimental results. This indicates that the mesh is of high quality.

$$\frac{\partial u}{\partial x} + \frac{\partial v}{\partial y} + \frac{\partial w}{\partial z} = 0 \quad (2.24)$$

$$\rho \left(u \frac{\partial u}{\partial x} + v \frac{\partial u}{\partial y} + w \frac{\partial u}{\partial z} \right) = -\frac{\partial p}{\partial x} + \mu \left(\frac{\partial^2 u}{\partial x^2} + \frac{\partial^2 u}{\partial y^2} + \frac{\partial^2 u}{\partial z^2} \right) + \rho g_x \quad (2.25)$$

$$\rho \left(u \frac{\partial v}{\partial x} + v \frac{\partial v}{\partial y} + w \frac{\partial v}{\partial z} \right) = -\frac{\partial p}{\partial y} + \mu \left(\frac{\partial^2 v}{\partial x^2} + \frac{\partial^2 v}{\partial y^2} + \frac{\partial^2 v}{\partial z^2} \right) + \rho g_y \quad (2.26)$$

$$\rho \left(u \frac{\partial w}{\partial x} + v \frac{\partial w}{\partial y} + w \frac{\partial w}{\partial z} \right) = -\frac{\partial p}{\partial z} + \mu \left(\frac{\partial^2 w}{\partial x^2} + \frac{\partial^2 w}{\partial y^2} + \frac{\partial^2 w}{\partial z^2} \right) + \rho g_z \quad (2.27)$$



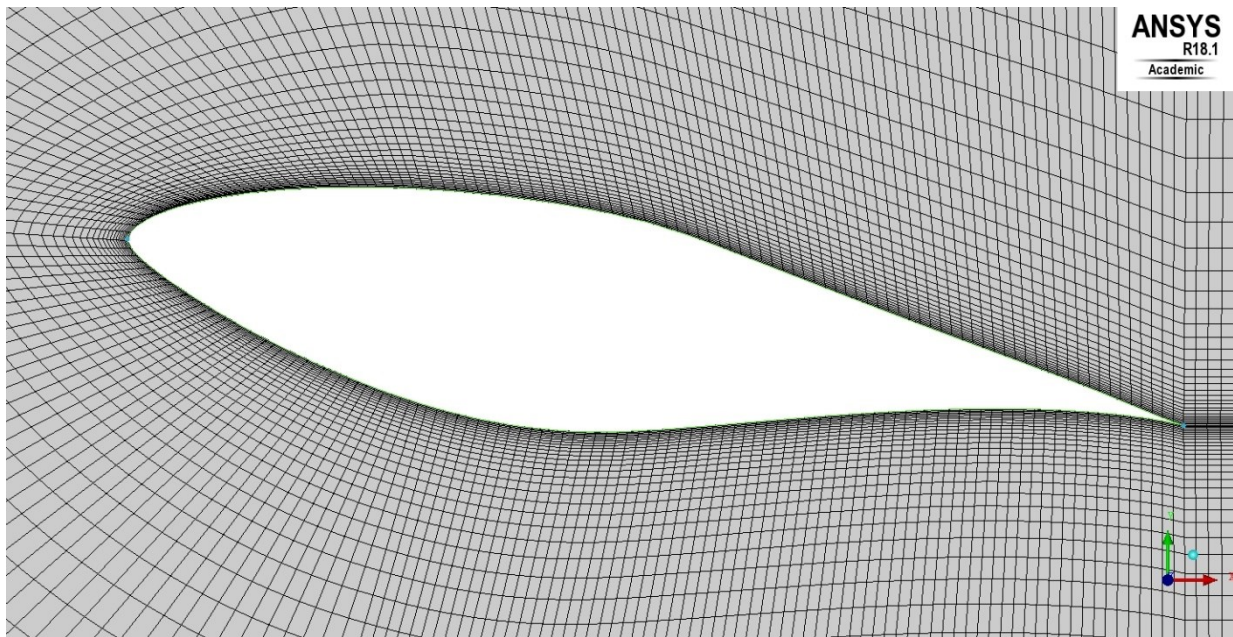
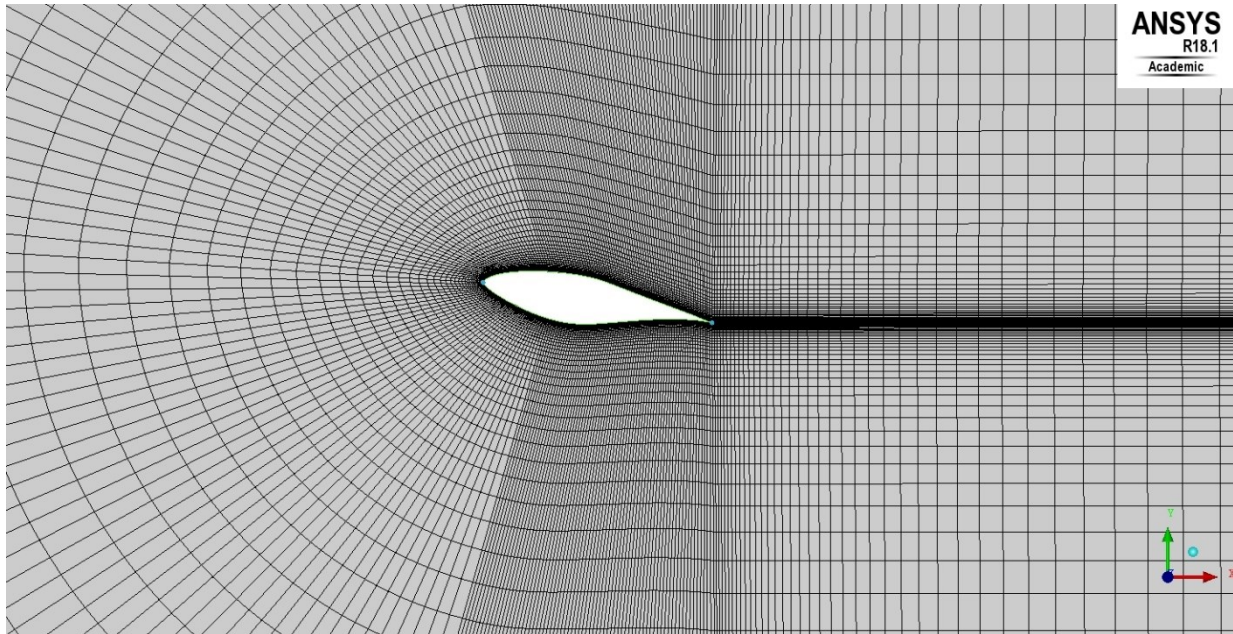


Figure 39. Grid around the airfoil

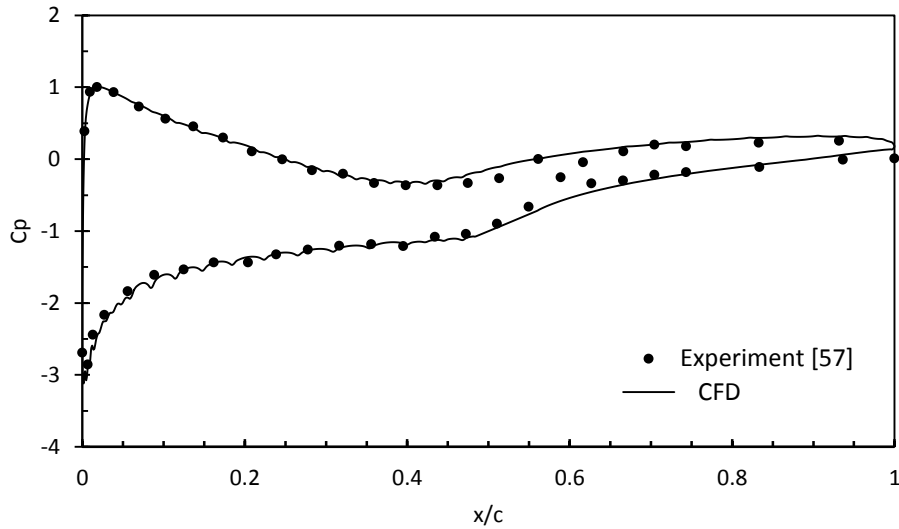


Figure 40. Coefficient of pressure for $\alpha = 9^\circ$ at $Re=1$ million

3.5 FSI model

3.5.1 CFD model

For a rotating wind turbine blade, as illustrated in Figure 41, the relative wind velocity vector has both x and y components. To consider the rotation of the blade in the CFD model, an inlet velocity profile is implemented in Fluent. The profile has constant x component equal to real wind velocity for all of the domain. However, the y component linearly increases from root to tip as a function of coordinate z. The magnitude of y component is equal to $R\Omega$ at the tip, where R is the blade length and Ω is the rotor rotational velocity.

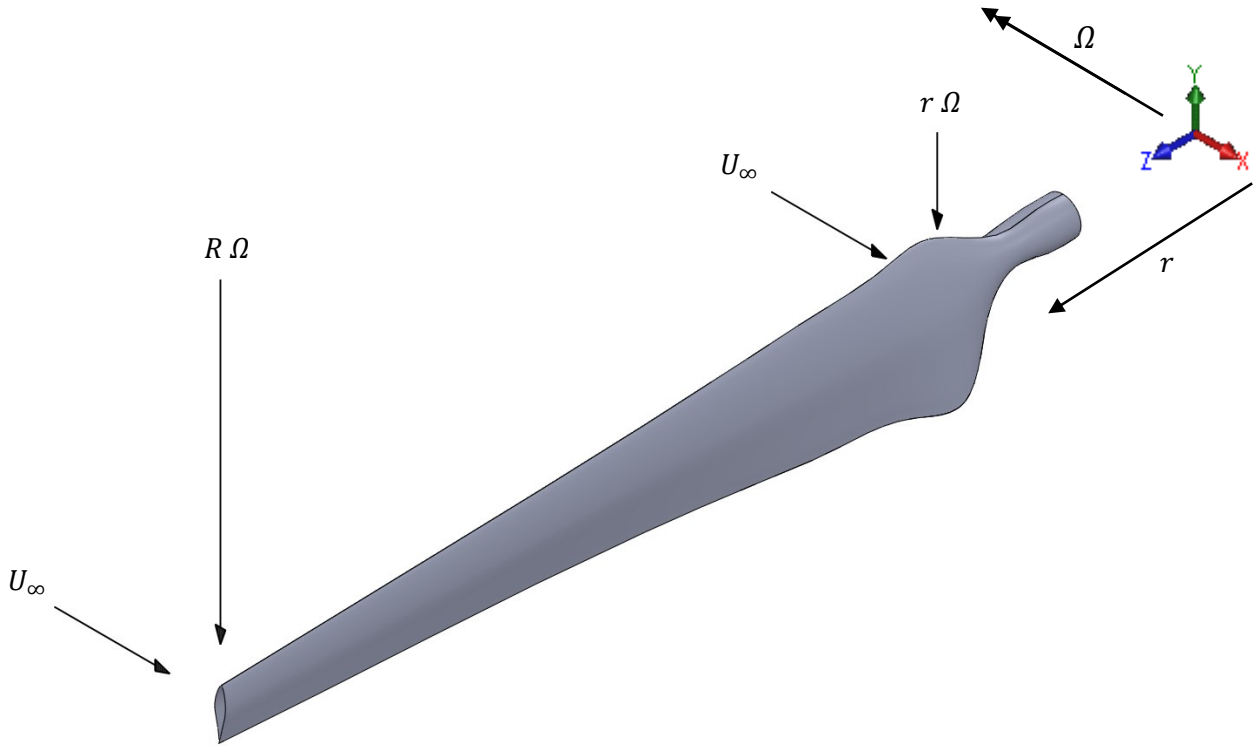


Figure 41. Wind velocity vectors on the blade

The use of the inlet velocity profile involves having angled vectors of velocity entering the domain through the inlets. In a C-grid as shown in Figure 42, this results in the flow exiting from the inlet at the top parts of the curved section, especially around the root of the blade where the relative velocity vector is angled steeper. To address this concern, the C-grid is incorporated in a rectangular domain as illustrated in Figure 43. The new grid is still structured, however, all boundaries are straight lines. Total number of 1,081,038 cells are used in the rectangular domain. Mesh independence study for the rectangular domain grid is presented in Table 7. Turbulence model $k - w$ is used in FSI model as it has been widely used in the studies of wind turbine blades [58, 59].

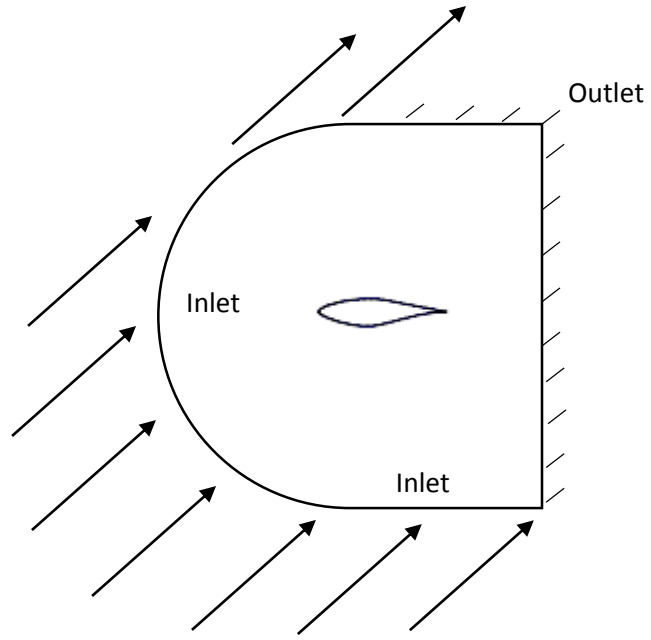
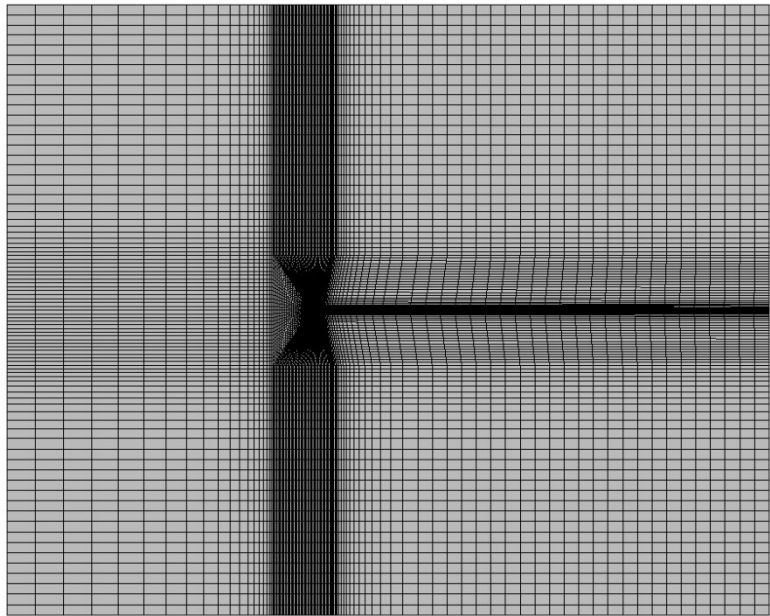
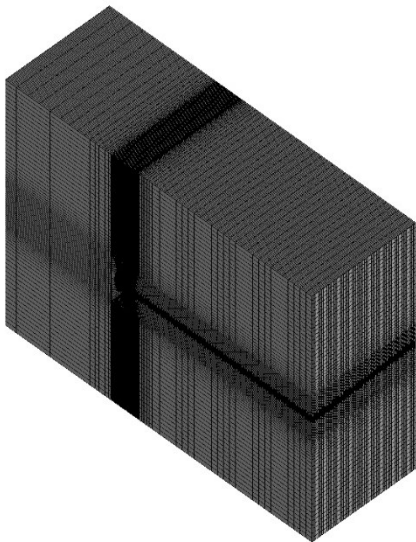


Figure 42. C-domain and boundary conditions



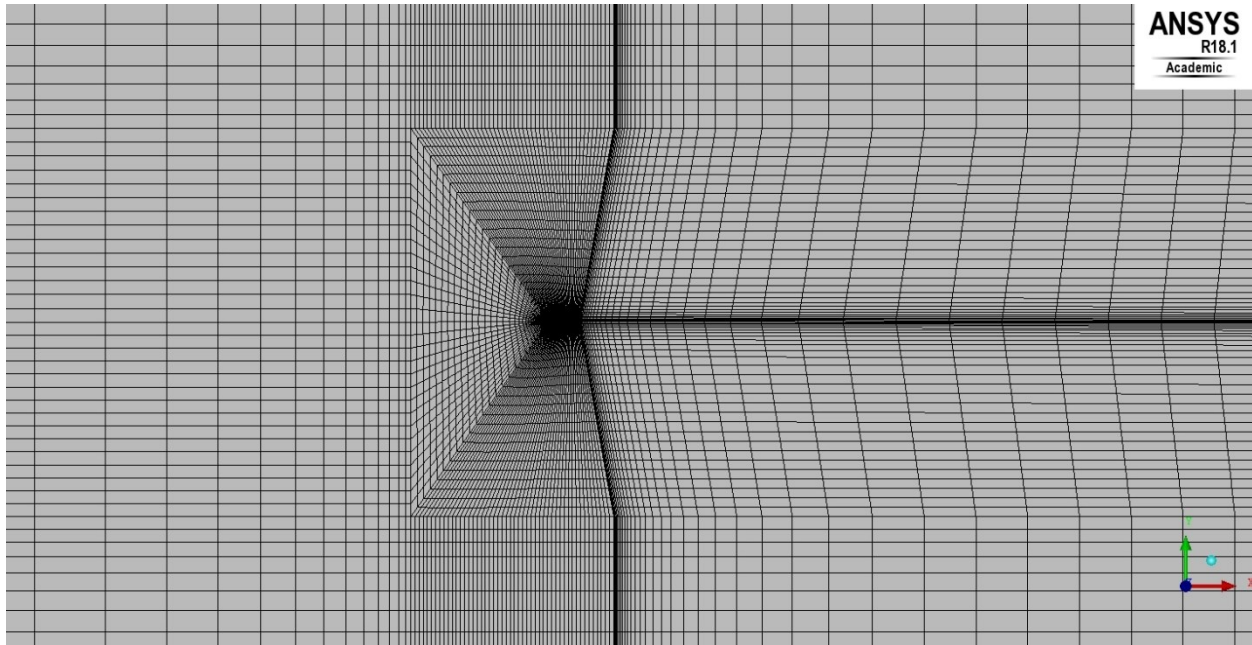


Figure 43. Rectangular domain mesh

Table 7. Mesh independence study for the 3D rectangular domain

Number of cells	Number of nodes on the airfoil	First layer thickness (mm)	Number of nodes along the blade span	Number of nodes in radial distance from the airfoil	Lift force (N)	Drag force (N)
377858	78	10	30	15	591.96	-12.80
654108	101	10	40	20	589.78	-20.08
1081038	131	8	50	30	593.96	-25.71

3.5.1.1 3D mesh verification

For a blade with taper, twist and variable inlet velocity, each section has a different Reynolds number and angle of attack. Reynolds number and angle of attack are calculated for each blade section over a range of inlet wind velocities. The section at $r = 4.275$ m with $Re = 10^6$ for which experimental data are available is selected for verification. CFD mesh verification is done using the pressure coefficient around the section. Figure 44 compares CFD results with experimental data. There is good agreement between CFD and experimental data in majority of

the section, except for the very tip of the airfoil on the suction side where the CFD model underestimates the pressure.

Underestimation of pressure at the tip of the airfoil on the suction side could be due to the insufficient mesh quality around the blade tip. The flow experiences abrupt change in direction while passing over the suction side at a high angle of attack. This rapid change of direction generally needs finer grid for more accurate calculation. Also, the results presented in Figure 44 are from a section of the blade where the airfoil has a 15° angle of attack which is much higher than its critical angle of attack of 10° . This results in flow separation and turbulence on the suction side of the airfoil. Significant quantities of turbulence makes a very complex flow condition therefore, makes it difficult to accurately predict the flow velocity and pressure. This can reduce the accuracy of the estimated coefficient of pressure. Coefficient of pressure for the same airfoil at a lower angle of attack (9°) is presented in Fig. 40. The numerical predictions have very good agreement with experimental data as at lower angles of attacks turbulence is not significant.

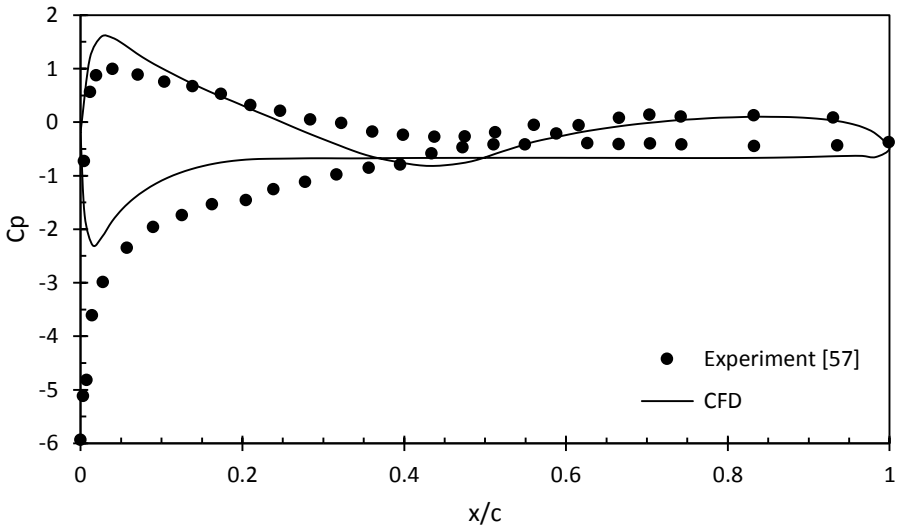


Figure 44. Coefficient of pressure for $\alpha = 15^\circ$ at $Re=1$ million

3.5.2 FE Model

The rotational forces from the blade weight are applied on the blade. The resulting force is calculated from the rotational velocity and applied as a body force on the blade (to represent blade rotation). Although the blade rotation is not defined in the domain, its effects are taken into account by using the velocity profile in CFD and rotational force load in FEA. There are 187,357 nodes and 188,165 elements used in the FE model. The elements are of the type Shell181. Figure 45 shows the quadrilateral elements on the blade skin. The same equivalent material that is used in analyzing the angle beam in Section 3.1 is used for the entire blade. The equivalent material properties are calculated based on several modal analyses of NREL Phase VI blade with composite materials. A study [56] finds that a blade with elasticity modulus of $E = 1.56 \times 10^{10}$ pa and poisson's ratio of $\nu = 0.42$ in all directions, have the same response from the composite blade. Therefore, these properties are considered as equivalent material properties and are used in this thesis for the blade simulation. Blade skin has constant thickness of 10^{-3} m and the spar thickness linearly decreases from 10^{-2} m at the root to 10^{-3} m at the tip. In the thicker model (results are presented in Section 3.7), the spar thickness is doubled.

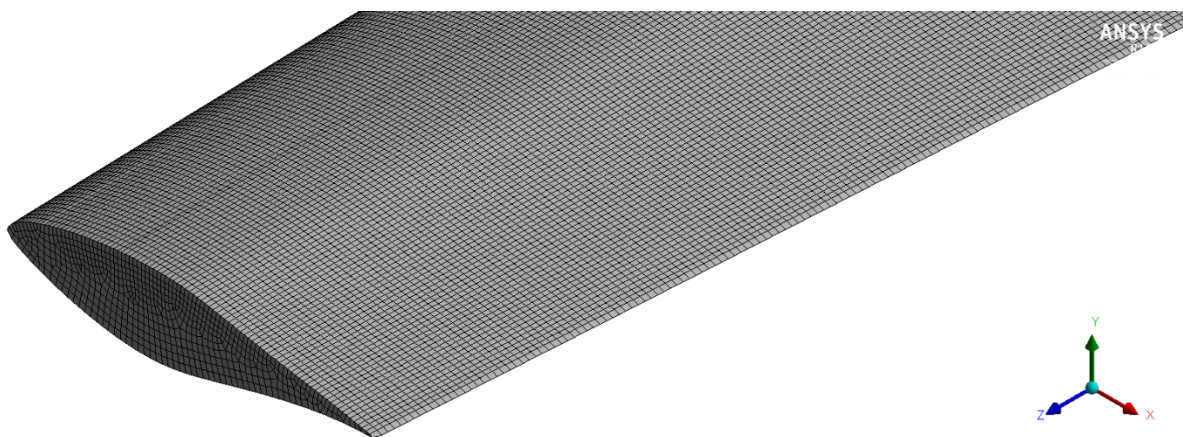
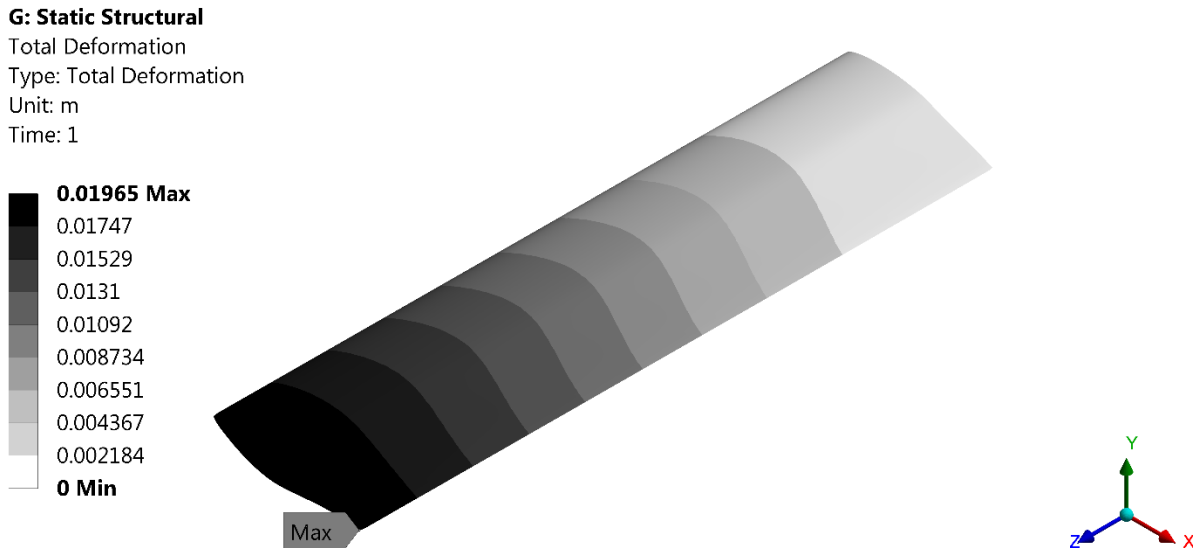


Figure 45. Blade mesh

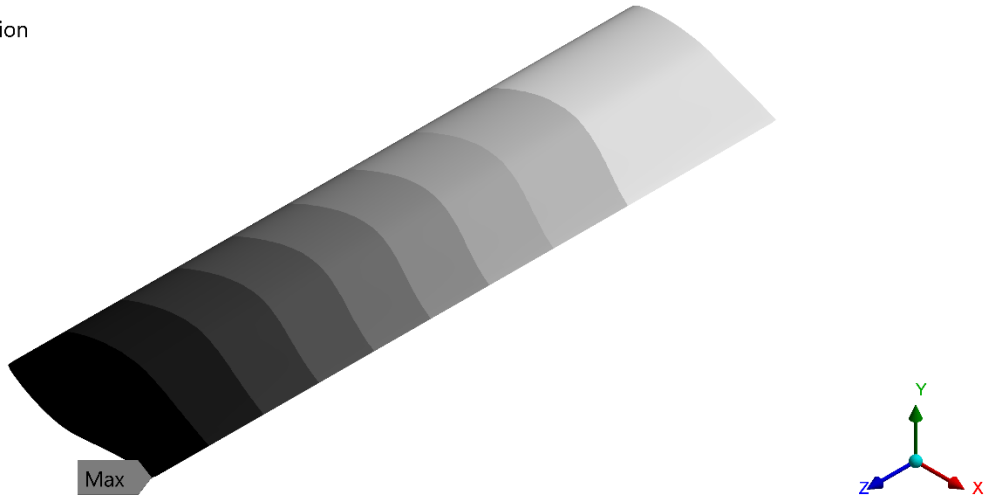
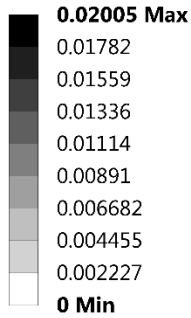
3.6 Two-way Vs. one-way FSI

Two-way FSI models are computationally costly so it is typically desirable to simplify them to one-way models if it is a reasonable assumption. To determine if this assumption is valid in this study, a two-way and a one-way model with same boundary conditions and loading are conducted and the results compared. For simplicity the blades are modeled without twist and taper. The wind velocity is set to 40 m/s. The deformed blades from both models are shown in Figure 46. Maximum deflection at the tip of the blade is 0.02 m in the two-way model, this number is 0.0196 m in the one-way model. The error of 2% is acceptable and a good compromise between accuracy and complexity. Therefore, one-way models are used for the rest of the study.



(a) One-way

E: Static Structural
Total Deformation
Type: Total Deformation
Unit: m
Time: 30



(b) Two-way

Figure 46. Blade deformation.

3.7 Elastic twist

In this section, fluid structure interaction results are presented for different spar locations, thicknesses and wind speeds. Induced elastic twist is the main variable that is investigated. To investigate the effect of wind speed on the induced elastic twist, the one way FSI model was performed for three different wind speeds. As illustrated in Figure 47, elastic twist is proportional to wind speed. The elastic twist is greater at the blade tip, which is expected as those parts are further from the fixed support boundary condition applied at the root of the blade. Elastic twist shows a linear increase along the span with an increased slope for higher wind speeds.

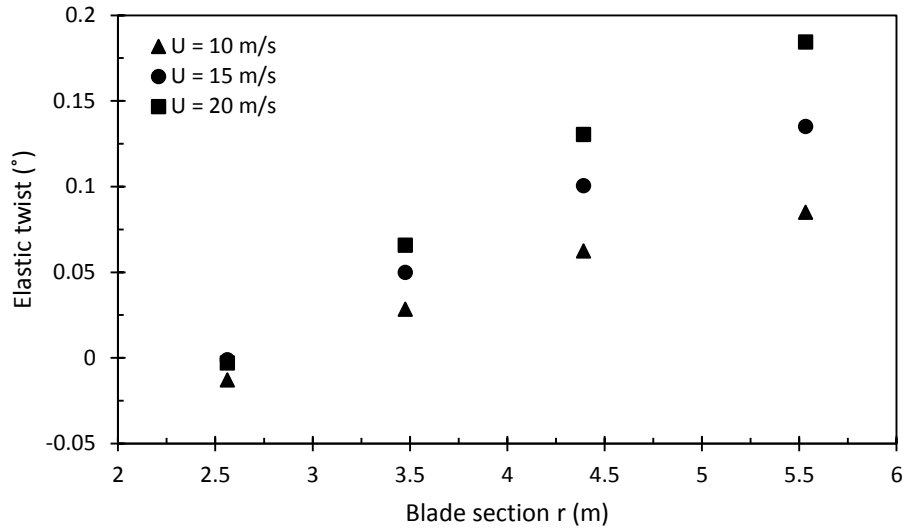


Figure 47. Induced elastic twist for different wind speeds for spar located at $x = 0.2c$

To investigate the effect of spar location on the induced twist, two models are compared. One with spar located at $x = 0.1c$ and the other one at $x = 0.2c$. Figure 48 compares the elastic twists for these two models. The model with the spar placed closer to the leading edge (thus further from the center of pressure) is showing more twist. This behavior is expected as a greater lever arm provides greater torque. However, it should be noted that due to constraints from airfoil geometry, the model with the spar placed closer to the leading edge has a spar which is shorter in height.

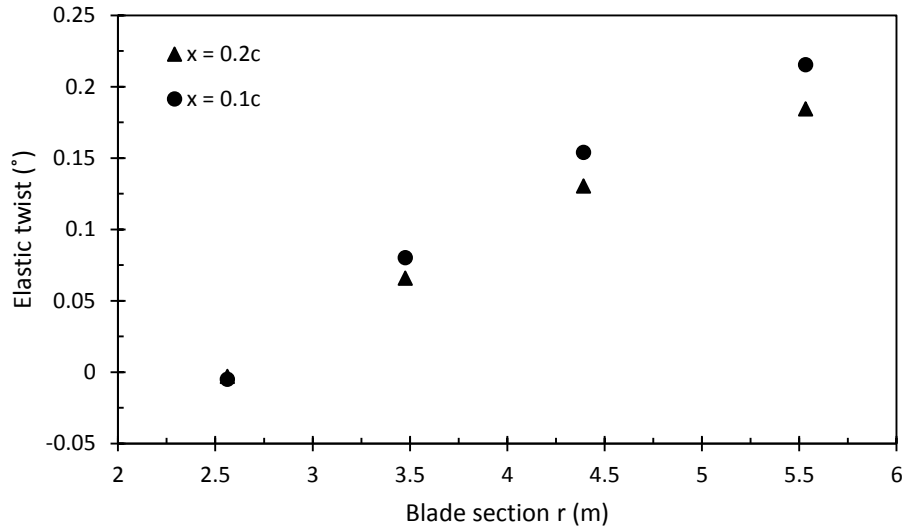


Figure 48. Elastic twist for different spar locations at $U_\infty = 20$ m/s

Spar thickness is also studied and the results are presented in Figure 49. A spar which is twice as thick, shows much more twist at each blade section. This is in contrast to a thicker spar having more torsional stiffness, thus should better resist torsion. An explanation for this could be that when the spar thickness is much greater than the skin thickness, the closed section's effect from the blade skin becomes much weaker. Therefore, the skin cannot develop a shear flow circuit and take up part of the torque. A much thinner blade skin eliminates the shear flow developed in the skin.

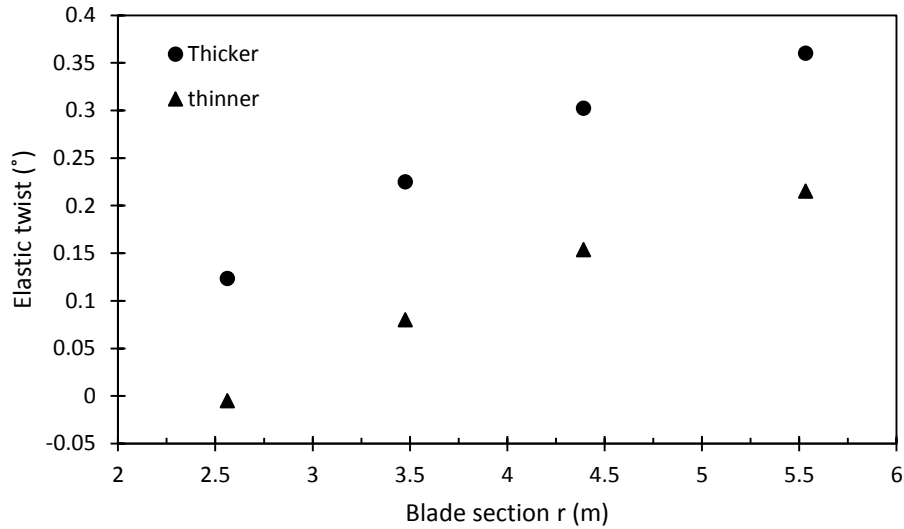


Figure 49. Effect of thickness on elastic twist. $x = 0.1c$, $U_\infty = 20$ m/s

3.8 Swept blade

3.8.1 Curved planform

To improve elastic twist of the blade, a curved design is employed. A modified swept blade is modeled based on the NREL Phase VI rotor and FSI analysis is conducted incorporating different types of spars. In this section, the results of bend induced twist for sweep blades are presented and compared between different models.

To form the curved planform of the blade, a power curve of order 4 is used and normalized to provide the desired bend depth at the tip. Bend depth is the perpendicular distance of the tip of the blade measured at 30% chord to the pitch axis of the blade. Two bend depths of 1 m and 1.5 m are studied. Figure 50 is the planform of the modified NREL Phase VI rotor blade. All of the other characteristics of the blade are maintained the same so the information on the blade can be found in Table 1, Figure 17 and Figure 18. Figure 51 illustrates the curved blade model with box spar.

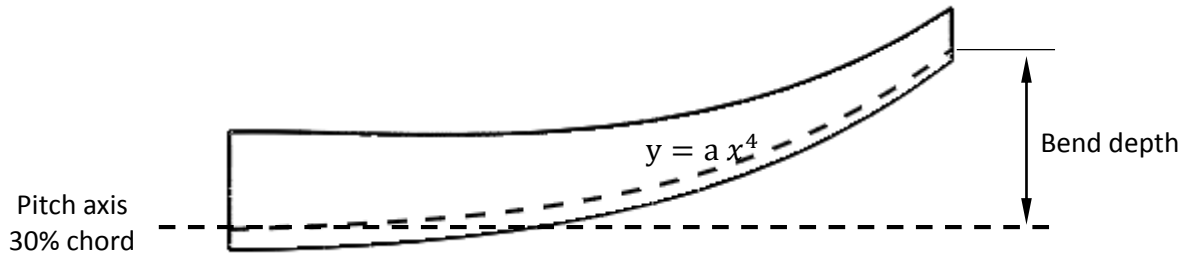


Figure 50. Modified curved blade planform

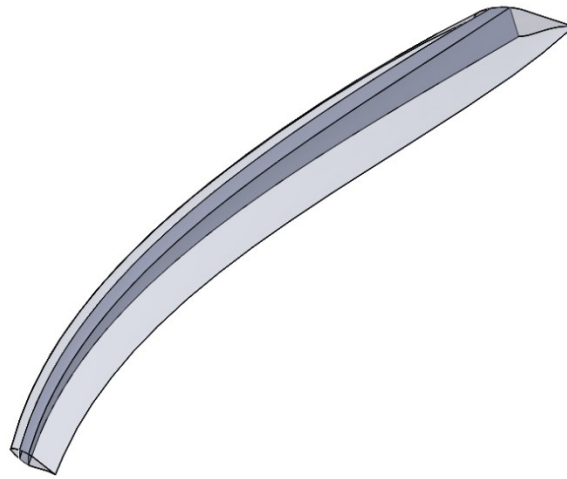


Figure 51. Swept blade with box spar

Unlike the previous models, the orientation of L spar facing leading edge is selected. This change is made because it will provide a larger shear web with greater bending stiffness. As box spar has greater bending stiffness, this selection helps in comparing the two model in a similar condition. Figure 52 is an illustration of the blade's cross sections.

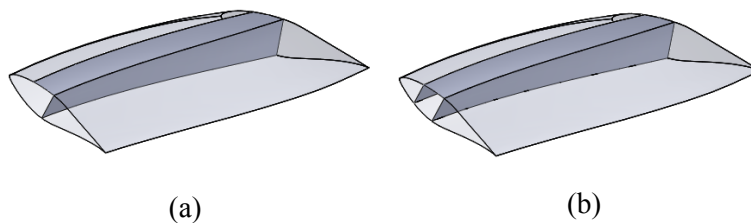


Figure 52. Cross section of the blade with (a) L spar and (b) Box spar

3.8.2 Elastic twist

FSI analysis is performed on the models for two wind velocities 10 m/s and 15 m/s. Figure 53 illustrates contours of flapwise deformation for the blade with box spar at $U_\infty = 15$ m/s. The undeformed blade is also shown in wireframe for comparison. A maximum of 4.5 cm of deflection is at the tip of the blade. The resultant induced elastic twist for different sections of the blade are presented in Figure 54. For better comparison, more plots with fewer series of data are presented and discussed in the rest of this section.

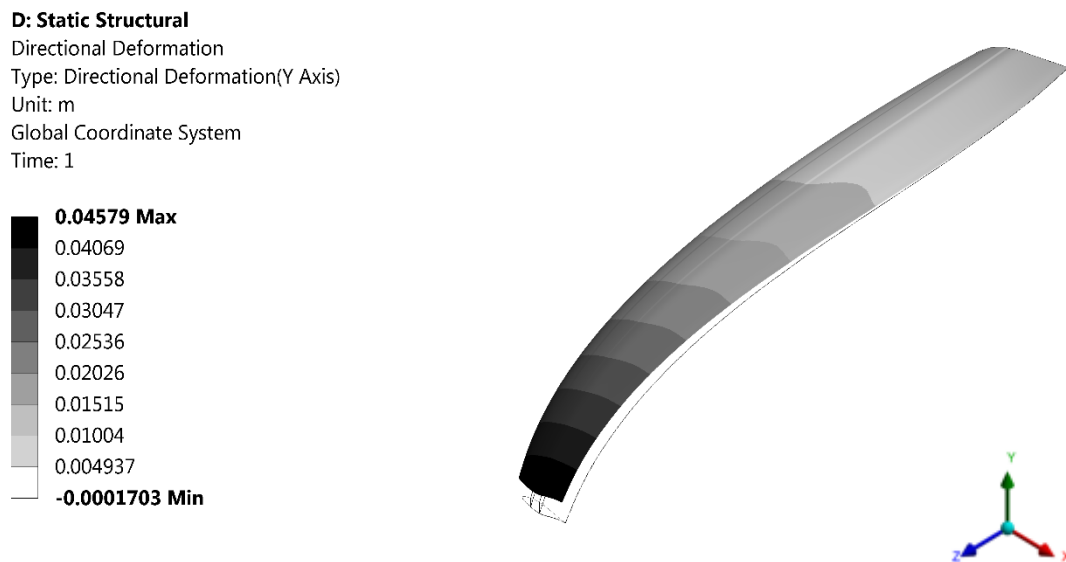


Figure 53. Flapwise bending

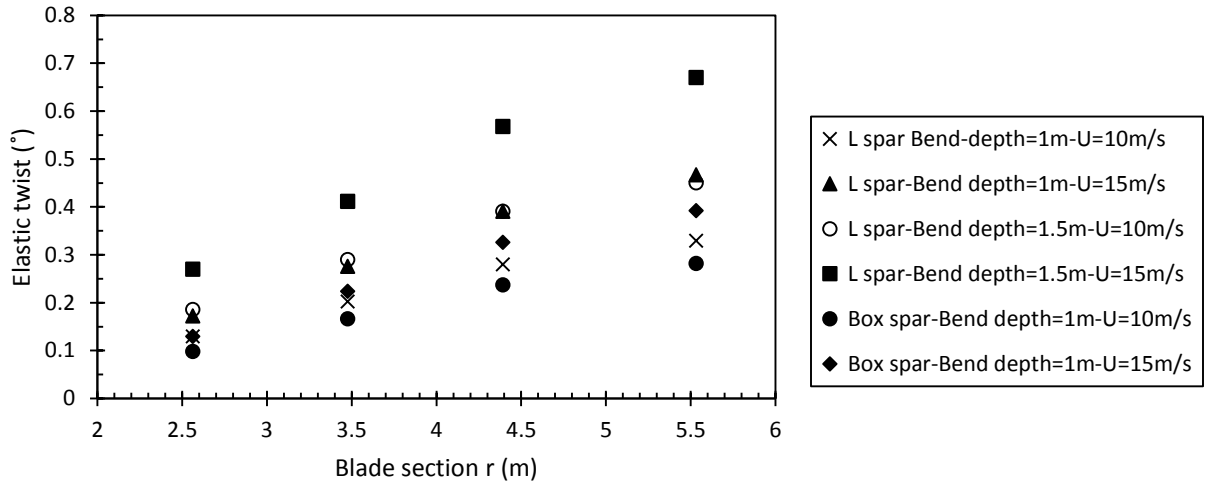


Figure 54. Elastic twist for swept blades

As illustrated in Figure 55, similar to the straight blade models, induced elastic twist is greater at higher wind speeds in the swept blade model. The effect of bend depth on elastic twist is presented in Figure 56 and Figure 57. There is a significant increase in elastic twist due to the blade curvature as illustrated in Figure 56 and Figure 57. Twist angle of up to 0.45° can be achieved with a bend depth of 1.5 m. An average increase of 41% in elastic twist can be achieved with 50% increase in bend depth at the rated wind speed 10 m/s. However, a blade with sharper curve planform is generally more expensive to build and the power gains might not offset the manufacturing costs.

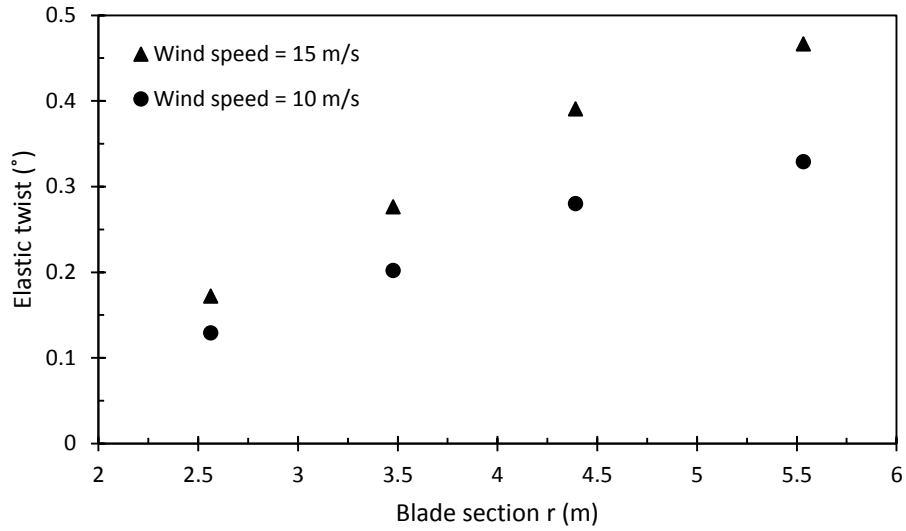


Figure 55. Induced twist of blade with L spar and bend depth of 1 m

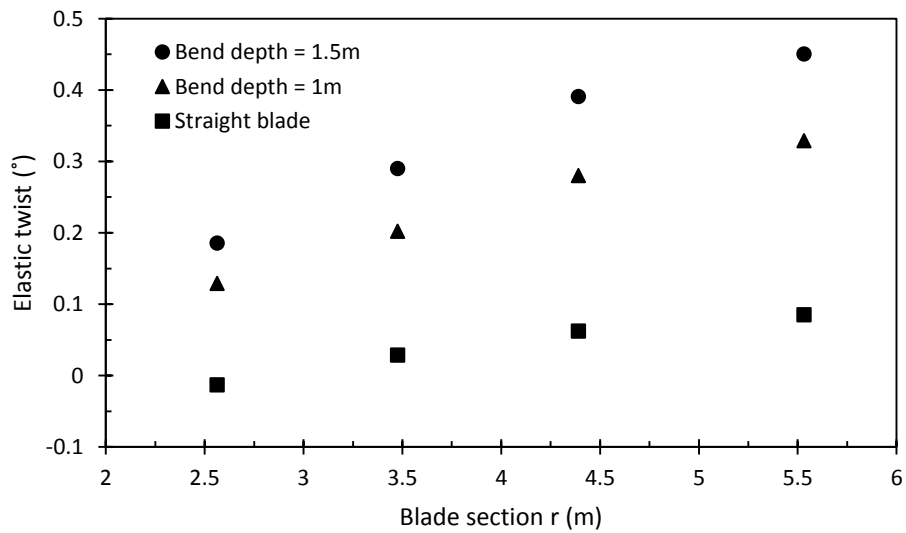


Figure 56. Induced twist of blade with L spar at $U_\infty = 10$ m/s

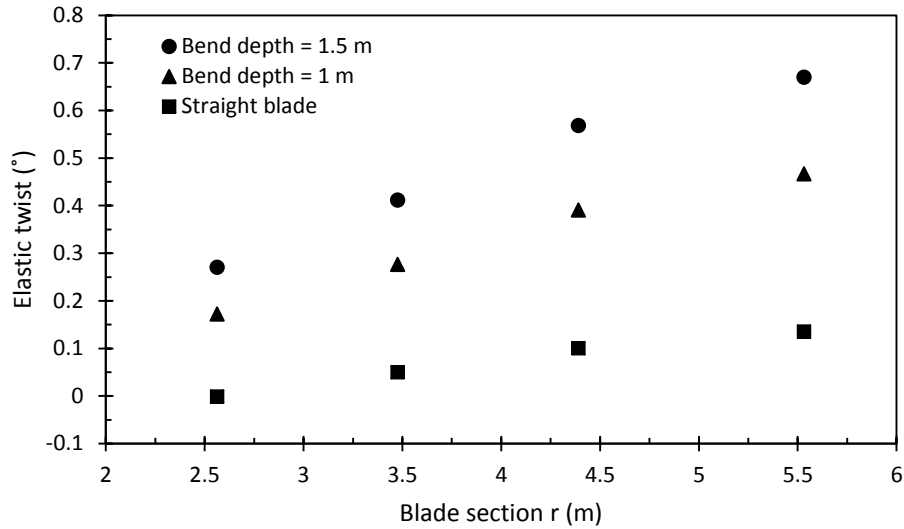


Figure 57. Induced twist of blade with L spar at $U_\infty = 15$ m/s

The blade with box spar shows less elastic twist compared to a blade with L spar. This is highlighted in Figure 58 and Figure 59. A box spar allows for the formation of a shear flow circuit that will resist torsion and part of the torque resulting in less elastic twist. The advantage of using an L spar over a box spar is that the blade with L spar experiences 18% more elastic twist. However, from other design criteria, a box spar might have superiority as it provides more stability in vibrations during wind fluctuations. Box spar needs to be analyzed from other mechanical aspects in future studies. The blade with box spar experiences less flapwise deformation because a box spar has greater bending stiffness compared to an L spar which has a single shear web.

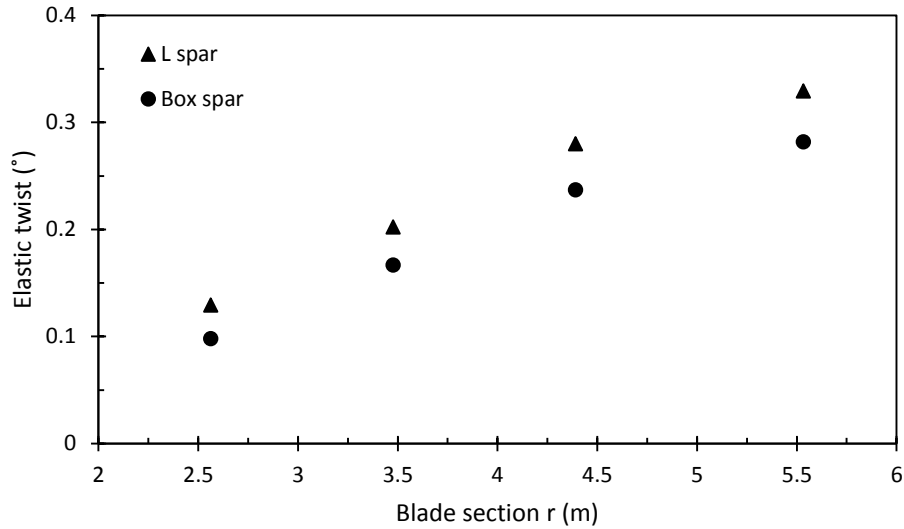


Figure 58. Induced twist for bend depth = 1 m at $U_\infty = 10$ m/s

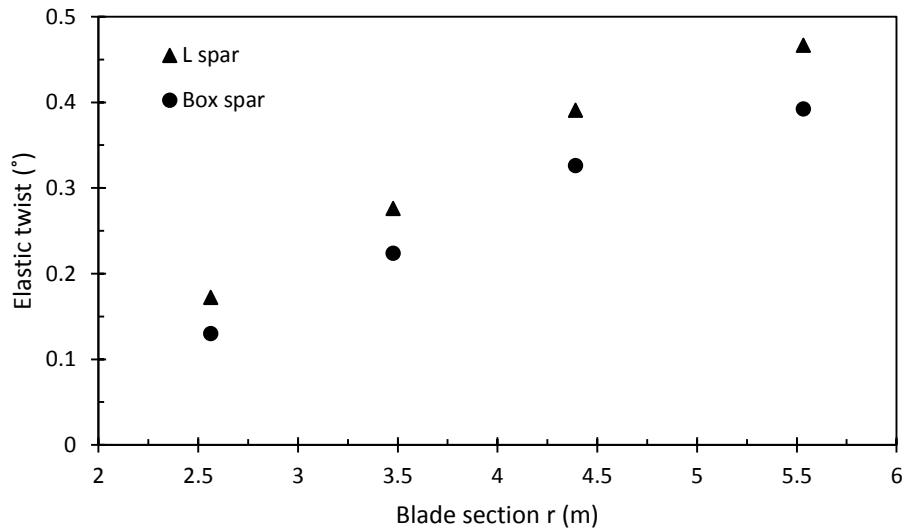


Figure 59. Induced twist for bend depth = 1 m at $U_\infty = 15$ m/s

3.8.3 Comparison of predicted elastic twist with optimal twist angle

As illustrated in Figure 60, optimal elastic twist and predicted elastic twist (from fluid structure interaction analysis) are compared for a wind speed of 10 m/s. In this analysis, approximately a 6-fold increase in the predicted elastic twist is needed to achieve optimal elastic twist at this wind speed at the tip of the blade. However, the optimal values for elastic

twist are obtained from an unrealistic and ideal rotor that is assumed to be able to twist each blade section significantly and non-monotonically, as illustrated in Fig. 60. This is impractical, however, setting feasible target curves instead can be a better reference frame to evaluate how effective bend-twist coupling modifications are. Further improvement in elastic twist might be possible to achieve by employing other types of BTC, such as biased fibers. Improvement in material properties also might lead to manufacturing blades that are more flexible while strong enough to be used in wind turbine blades.

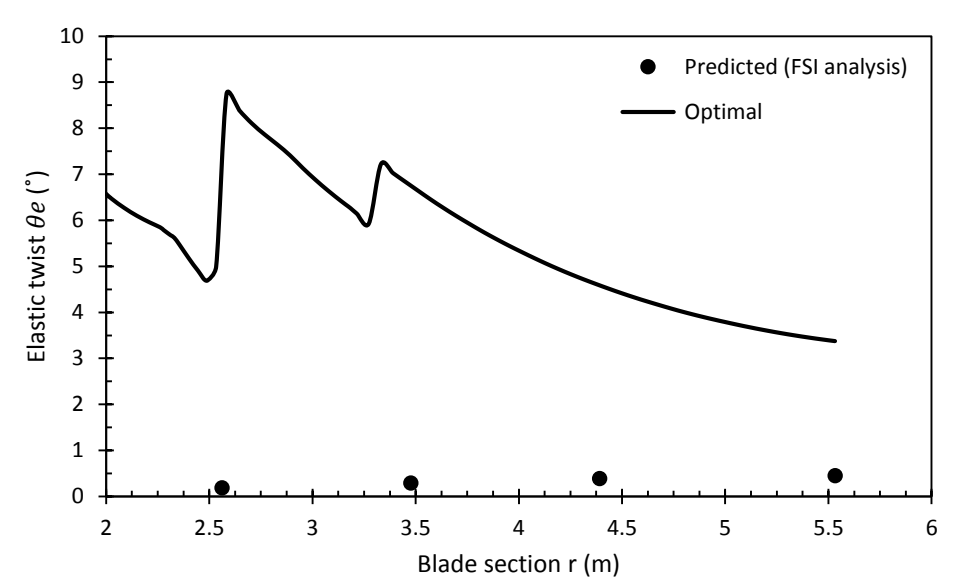


Figure 60. Elastic twist for blade with bend depth of 1.5 m and L spar at $U_\infty = 10$ m/s

3.8.4 Power increase

After obtaining θ_e 's from FSI analysis, a modification is done on the code to be able to calculate the resultant power increase. As presented in the Section 2.1, elastic twist adds to each section's pitch angle and changes the angle of attack. Under the new condition, the performance of the turbine will change. At wind speed $U_\infty = 10$ m/s, the power generation increases by 1.89%. However, a power reduction is seen for a lower wind speed, i.e., $U_\infty = 5$ m/s.

As illustrated in Figure 20, for 5 m/s wind speed, the elastic twist needs to be in opposite direction (nose up), in contrast with higher wind speed 8 m/s that a nose down twist is needed.

Table 8. Power change

U_{∞} (m/s)	Power (kW)		Change (%)
	Solid blade	BTC	
10	11.35	11.56	1.89
5	3.505	3.250	-7.26

Although the power improvement might seem relatively small, the 1.89% calculated increase is for the rated speed and when considered throughout the total lifetime of a blade, will result in significantly more power production. Also, this improvement comes with relatively small changes in the design and manufacturing process of the blade making it more desirable. Ultimately, the power improvement can be considered as proof of concept for further studies.

4 Conclusions and recommendations

4.1 Conclusions

Power optimization for a wind turbine blade was done based on BEMT and power enhancement capacities were confirmed. An elastic twist of up to 5° is needed for optimal power enhancement purposes around the rated wind speed. Aeroelastic capacities of a blade with an L spar were studied through fluid-structure interaction analysis. The results show up to 0.36° elastic twist for a thick configuration of the spar at higher wind speeds. Two spar thickness configurations were studied while the same blade skin thickness was maintained. The FSI results indicate there is more elastic twist in the thicker configuration. Elastic twist is improved with the spar placed closer to the leading edge of the blade.

Elastic twist resulted from the FSI analysis were compared to desired elastic curves. It was found that although some elastic twists is predicted, it is not comparable to the amounts needed for optimal power output. As a result, the curved planform blade was combined with L spar to enhance the elastic twists. The results show improved elastic twist in the modified swept blades. For a bend depth of 1.5 m, elastic twists of up to 0.67° were predicted at 15 m/s wind speed. Swept blades with L spar and box spar were modeled, analyzed and compared. The results indicate the blade with L spar yields considerably more elastic twist compared to the blade with box spar. Power increase of 1.89% was predicted from the elastic twists in the swept blade with L spar at the rated wind speed 10 m/s.

4.2 Recommendations for future studies

Elastic twist can also be optimized for load alleviation purposes. Stall characteristics of the blade can be improved by nose up elastic twist resulting in lower gust loads. A nose up elastic twist helps with putting the sections of the blade into stall at more optimal wind speeds. Nose up elastic twist can be obtained using a reverse swept planform (forward). Also, combining geometry BTC with material BTC can be studied for higher orders of elastic twists. A blade with L spar, swept planform and biased fibers in the spar and skin provides more potential for bend-twist coupling. Transient analysis to study the blade response in wind fluctuations is also a topic of interest. A transient analysis can reveal how fast BTC can be in responding to wind fluctuations.

References

- [1] Population Division, Department of Economic and Social Affairs, "World Population Prospects," United Nations, New York, 2017 Revision.
- [2] International Energy Agency, "Key world Energy Statistics," Paris, 2017.
- [3] International Energy Agency, "Key World Energy Statistics," Paris, 2010.
- [4] NASA, "Global Climate Change - Global Temperature," [Online]. Available: <https://climate.nasa.gov/vital-signs/global-temperature>. [Accessed 22 May 2018].
- [5] T. Burton, N. Jenkins, D. Sharpe and E. Bossanyi, Wind Energy Handbook, West Sussex: Willey & Sons, 2011.
- [6] S. J. Johnson, C. P. van Dam and D. E. Berg, "Active load control techniques for wind turbines," Sandia National Laboratories, Albuquerque, 2008.
- [7] Committee on Assessment of Research Needs for Wind Turbine Rotor Materials Technology, Energy Engineering Board, Commission on Engineering and Technical Systems, National Research Council, Assessment of research needs for wind turbine rotor materials technology, Washington, D.C.: National Academy Press, 1991.
- [8] E. J. Novaes Menezes and A. M. Araujo, "A review on wind turbine control and its associated methods," *Journal of Cleaner Production*, vol. 174, pp. 945-953, 2018.
- [9] Energy Unlimited Inc., "Variable Length Wind Turbine Blade," U.S. Department of Energy, Office of Scientific and Technical Information, Oak Ridge, TN, 2006.
- [10] GE Wind Energy, LLC, "Advanced Wind Turbine Program Next Generation Turbine Development Project," Subcontract Report NREL/SR, 2006.

- [11] R. N. Sharma and U. K. Madawala, "The concept of a smart wind turbine system," *Renewable Energy*, vol. 39, pp. 403-410, 2012.
- [12] S. V. Pasupulati, J. Wallace and M. Dawson, "Variable Length Blades Wind Turbine," in *Power Engineering Society General Meeting IEEE*, San Francisco, CA, 12-16 June, 2005.
- [13] M. Imraan, R. N. Sharma and R. G. J. Flay, "Wind tunnel testing of a wind turbine with the telescopic blades: the influence of step change in chord," in *17th Australian Fluid Mechanics Conference*, Auckland, New Zealand, 5-9 December, 2010.
- [14] D. T. Yen, C. P. van Dam, F. Bräeuchle, R. L. Smith and S. D. Collins, "Active Load Control and Lift Enhancement Using MEM Translational Tabs," in *Fluids 2000 AIAA-2422*, Denver CO, 19-22 June 2000.
- [15] D. T. Yen Nakafuji, C. P. van Dam, R. L. Smith and S. D. Collins, "Active Load Control for Airfoils Using Microtabs," *Journal of Solar Energy Engineering*, vol. 123, no. 4, pp. 282-289, 2001.
- [16] D. T.-L. Yen, Active Load Control using Microtabs, PhD. dissertation, University of California, Davis, CA, 2001.
- [17] K. J. Standish and C. P. van Dam, "Computational Analysis of a Microtab-Based Aerodynamic Load Control System for Rotor Blades," *Journal of the American Helicopter Society*, vol. 50, no. 3, pp. 249-258, 2005.
- [18] C. P. van Dam, K. j. Standish and J. P. Baker, "Computational and Experimental Investigation into the Effectiveness of a Microtab Aerodynamic Load Control System," Sandia Report AO273, Aug. 2004.
- [19] A. Ebrahimi and M. Movahhedi, "Wind turbine power improvement utilizing passive flow control with microtab," *Energy*, vol. 150, pp. 575-582, 2018.
- [20] M. H. Shirk, T. J. Hertz and T. A. weisshaar, "Aeroelastic Tailoring – Theory, Practice, Promise," *Journal of Aircraft*, vol. 23, no. 1, pp. 6-18, 1986.

- [21] R. H. Blackwell, "Blade Design for Reduced Helicopter Vibration," *Journal of the American Helicopter Society*, vol. 28, no. 3, pp. 33-41, 1983.
- [22] Weisshaar, *Aircraft Aeroelastic Design and Analysis*, School of Aeronautics and Astronautics, Purdue University, 1995.
- [23] P. Veers, G. Bir and D. W. Lobitz, "Aeroelastic Tailoring in Wind-Turbine Blade Applications," in *Windpower '98 American Wind Energy Association Meeting and Exhibition*, Bakersfield, CA, April 28 - May 1, 1998.
- [24] D. W. Lobitz and P. Veers, "Aeroelastic Behavior of Twist-coupled HAWT Blades," in *ASME/AIAA Wind Energy Symposium*, Reno, NV, 1998.
- [25] D. W. Lobitz and D. J. Laino, "Load Mitigation with Twist-coupled HAWT Blades," in *ASME/AIAA 37th Aerospace Sciences Meeting and Exhibition*, Reno, NV, 1999.
- [26] D. W. Lobitz, P. S. Veers and D. J. Laino, "Performance of Twist-Coupled Blades on Variable Speed Rotors," in *ASME/AIAA Wind Energy Symposium*, Reno, NV, 2000.
- [27] D. W. Lobitz, P. S. Veers, G. R. Eisler, D. J. Laino, P. G. Migliore and G. Bir, "The Use of Twist-Coupled Blades to Enhance the Performance of Horizontal Axis Wind Turbines," Sandia Report, Albuquerque, NM, May 2001.
- [28] T. D. Ashwill, P. Veers, D. Griffin, J. Locke, I. Contreras and M. D. Zuteck, "Concepts for Adaptive Wind Turbine Blades," in *ASME/AIAA Wind Energy Symposium*, Reno, NV, 2002-0028.
- [29] T. D. Ashwill, "Passive Load Control for Large Wind Turbines," in *51st AIAA/ASME/ASCE/AHS/ASC Structures, Structural Dynamics, and Materials Conference*, Orlando, FL, April 2010.
- [30] M. Capuzzi, A. Pirrera and P. M. Weaver, "A novel adaptive blade concept for large-scale wind turbines. Part I: Aeroelastic behaviour," *Energy*, vol. 73, pp. 15-24, 2014.

- [31] M. Capuzzi, A. Pirrera and P. M. Weaver, "A novel adaptive blade concept for large-scale wind turbines. Part II: structural design and power performance," *Energy*, vol. 73, pp. 25-32, 2014.
- [32] M. Capuzzi, A. Pirrera and P. M. Weaver, "Structural design of a novel aeroelastically tailored wind turbine blade," *Thin-Walled Structures*, vol. 95, pp. 7-15, 2015.
- [33] F. Stoddard, V. Nelson, K. Starcher and B. Andrews, "Determination of elastic twist in horizontal axis wind turbines (HAWTs)," Subcontract Report NREL/SR-500-12087, June 2006.
- [34] D. J. Malcolm and A. C. Hansen, "WindPACT Turbine Rotor Design Study: June 2000-June 2002," Subcontract Report NREL/SR-500-32495, 2006.
- [35] D. W. Lobitz and P. S. Veers, "Load mitigation with bending/twist-coupled blades on rotors using modern control strategies," *Wind Energy*, vol. 6, pp. 105-117, 2003.
- [36] D. R. Verelst and T. J. Larsen, "Load Consequences when sweeping blades - a case study of a 5 MW pitch controlled wind turbine," Technical University of Denmark, Risø National Laboratory for Sustainable Energy, 2010.
- [37] D. Berry and A. T., "Design of 9-Meter Carbon-Fiberglass Prototype Blades: CX-100 and TX-100," Sandia Report SAND2007-0201, September 2007.
- [38] N. M. Karaolis, P. J. Mussgrove and G. Jeronimidis, "Active and passive aeroelastic power control using asymmetric fibre reinforced laminates for wind turbine blades," in *10th British Wind Energy Conference 163-172*, London, March 1988.
- [39] N. M. Karaolis, G. Jeronimidis and P. J. Mussgrove, "Composite wind turbine blades: coupling effects and rotor aerodynamic performance," in *EWEC '89 244-248*, Glasgow, 1989.
- [40] H. J. T. Kooijman, "Bending-torsion coupling of a wind turbine rotor blade," in *ECN report I-96-060*, Petten, December 1996.

- [41] D. W. Lobitz, P. S. Veers and P. G. Migliore, "Enhanced performance of HAWTs using adaptive blades," in *Proceedings of the 1996 ASME Wind Energy Symposium 41-45*, Houston, TX, January-February 1996.
- [42] C.-H. Ong and S. W. Tsai, "Design, Manufacture and Testing of a Bend-Twist D-Spar," Sandia National Laboratories SAND99-1324, Albuquerque, NM, June 1999.
- [43] M. D. Zuteck, "Adaptive Blade Concept Assessment: Curved Planform Induced Twist Investigation," Sandia National Laboratories SAND02-2996, Albuquerque, NM, 2002.
- [44] T. D. Ashwill, G. Kanaby, K. Jackson and M. Zuteck, "Development of the Swept Twist Adaptive Rotor (STAR) Blade," in *48th AIAA Aerospace Sciences Meeting*, Orlando, FL, 4-7 Jan 2010.
- [45] S. Larwood, C. P. van Dam and D. Schow, "Design studies of swept wind turbine blades," *Renewable Energy*, vol. 71, pp. 563-571, 2014.
- [46] J. L. Tangler, "The Nebulous Art of Using Wind-Tunnel Airfoil Data for Predicting Rotor Performance," in *the 21st ASME Wind Energy Conference*, Reno, Nevada, Jan 14-17, 2002.
- [47] M. M. Hand, D. A. Simms, L. J. Fingersh, D. W. Jager, J. R. Cotrell, S. Schreck and S. M. Larwood, "Unsteady Aerodynamics Experiment Phase VI: Wind Tunnel Test Configurations and Available Data Campaigns," National Renewable Energy Laboratory NREL/TP-500-29955, December 2001.
- [48] P. Roth-Johnson, R. E. Wirz and E. Lin, "Structural design of spars for 100-m biplane wind turbine blades," *Renewable Energy*, vol. 71, pp. 133-155, 2014.
- [49] T. H. G. Megson, *Aircraft Structures for Engineering Students*, London: Edward Arnold Ltd, 1972.
- [50] Q. Zhang and T. Hisada, "Studies of the strong coupling and weak coupling methods in FSI analysis," *International Journal for Numerical Methods in Engineering*, vol. 60, no. 12, pp. 2013-2029, 2004.
- [51] G. Hou, J. Wang and A. Layton, "Numerical Methods for Fluid-Structure Interaction - A Review,"

Communications in Computational Physics, vol. 12, no. 2, pp. 337-377, 2012.

- [52] C. A. Felippa, "Model Based Partitioned Simulation of Coupled Systems," in *Computational Aspects of Structural Acoustics and Vibration*, Springer-Verlag Wien, 2009, pp. 171-216.
- [53] C. Farhat and M. Lesoinne, "Two efficient staggered algorithms for the serial and parallel solution of three-dimensional nonlinear transient aeroelastic problems," *Computer Methods in Applied Mechanics and Engineering*, vol. 182, no. 3-4, pp. 499-515, 2000.
- [54] V. Jean-Marc, D. C. H. Pascal and L. Benoit, "Strong Coupling Algorithm to Solve Fluid-Structure-Interaction Problems with a Staggered Approach. Workshop on Simulation for European Space Programmes (SESP2010).," in *Workshop on Simulation for European Space Programmes (SESP2010), Modeling and Simulation Session*, Noordwijk, Netherlands, 30 sep, 2010.
- [55] Ansys 18.1 Documentaion.
- [56] K. Lee, Z. Huque and R. H. S.-E. Kommalapati, "Evaluation of equivalent structural properties of NREL phase VI wind turbine blade," *Renewable Energy*, vol. 86, pp. 796-818, 2016.
- [57] R. R. Ramsay, J. M. Janiszewska and G. M. Gregorek, "Wind Tunnel Testing of Three S809 Aileron Configurations for use on Horizontal Axis Wind Turbines, Airfoil Performance Report," National Renewable Energy Laboratory NREL , July 1996.
- [58] J.-O. Mo and Y.-H. Lee, "CFD Investigation on the aerodynamic characteristics of a small-sized wind turbine of NREL PHASE VI operating with a stall-regulated method," *Journal of Mechanical Science and Technology*, vol. 26, no. 1, pp. 81-92, 2012.
- [59] N. N. Sørensen, J. A. Michelsen and S. Schrek, "Navier–Stokes predictions of the NREL phase VI rotor in the NASA Ames 80 ft×120 ft wind tunnel," *Wind Energy*, vol. 5, no. 2-3, pp. 151-169, 2002.